The Dissertation Committee for Dustin Matthew Schroeder
certifies that this is the approved version of the following dissertation:

Characterizing the Subglacial Hydrology of Thwaites Glacier, West Antarctica Using Airborne Radar Sounding

Committee:

Donald D. Blankenship, Supervisor

R. Keith Raney

John B. Anderson

Omar Ghattas

Marc A. Hesse

David Mohrig

Characterizing the Subglacial Hydrology of Thwaites Glacier, West Antarctica Using Airborne Radar Sounding

by

Dustin Matthew Schroeder, B.A., B.S.E.E.

DISSERTATION

Presented to the Faculty of the Graduate School of

The University of Texas at Austin

in Partial Fulfillment

of the Requirements

for the Degree of

DOCTOR OF PHILOSOPHY

THE UNIVERSITY OF TEXAS AT AUSTIN

May 2014

To Don, whose commitment to curiosity, creativity, and compassion in interdisciplinary observational science provided as enriching an environment for graduate education as I am aware exists

&

Devon, with whom every area and endeavor of my life is immeasurably better

Acknowledgments

I wish to thank: N. Schroeder for teaching me to understand, design, and optimize physical systems. M. Fraschetti Schroeder for instilling me with the conviction that I could accomplish anything and first suggesting that I might like science. N. Haw for decades of collaborative thought experiments and first exposing me to the concepts of specular reflection and diffuse scattering when we were teenagers. D. Ross, B. Hines, and D. Kirian for introducing me to the experience of being part of a science and engineering team. C. Simpson, J. DeRocher, and J. Bishop for fostering my first interest in the natural world. D. Akerib for showing me that scientific research is actually something that people can do with their lives. D. L. Young and G. Putz for teaching me the importance of challenging and empowering young scientists. K. Marosi for enabling a liberal arts education in science and engineering. P. Reid for exposing me to the joy of scientific instrument design. S. Roy for showing me the power of a research group engaged in both science and engineering scholarship. D. Kelley for teaching me the importance of good lab notebooks and first introducing me to radar and antenna design. J. Patel for teaching me that industry can be a catalyst for education and intellectualism. S. Burrows for insisting that I belonged in geophysics, research, and the academy. D. Blankenship for teaching me to think like a geophysical glaciologist; treating instruments, observations, analysis, inference, and synthesis with equal intellectual respect. H. Ling for being a model of joy and creativity in electromagnetic scholarship.

J. Anderson for his wisdom and mentorship regarding academic geoscience. R. K. Raney for teaching me that radar science is a subject with history, nuance, and the potential for profound theoretical elegance. O. Ghattas, M. Hesse, and D. Mohrig for their insight, interest, and encouragement in my scientific, personal, and professional development. D. Ryan for convincing me of the importance of opinion, conviction, and the public in communicating science. A. Baker for insisting that doing great science requires producing great writing. G. Purves, R. Came, and W. Krauss for reminding me that observations, facts, theories, and scientists themselves have historical, cultural, and epistemological context and meaning. J. Greenbaum for challenging me to redefine greatness in teamwork, leadership, management, and exploration in the service of science and society. D. A. Young, E. Quartini, M. Cavitte, C. Grima, K. Soderlund, G. Ng, A. Witus, J. MagGregor, O. Sergienko, A. LeBrocq, G. W. Patterson, Y. Gim, M. Siegert, S. Kempf, A. Wright, R. Warner, D. Kichner, A. Ferro, A. Ilisei, D. Castelletti, W. Kofman, T. Richter, J. Roberts, B. Schmidt, J. Dowdeswell, L. Bruzzone, and A. Moussessian for their scientific, technical, and intellectual partnership. The members of the LASA High School Science Olympiad Team for being a constant source of inspiration and insight into the nature of teaching, learning, creativity, and excellence.

Characterizing the Subglacial Hydrology of Thwaites Glacier, West Antarctica Using Airborne Radar Sounding

Dustin Matthew Schroeder, Ph.D.
The University of Texas at Austin, 2014

Supervisor: Donald D. Blankenship

Hydrologic, lithologic, and geothermal basal boundary conditions can exert strong, even dominating, control on the evolution, stability, and sea level contribution of ice sheets and glaciers. However, the scales at which the physical processes and observable signatures of this control occur are typically smaller than the spatial resolutions currently achievable using ice penetrating radar. Further, the strength of radar bed echo returns is affected by the material and geometric properties of the bed as well as englacial attenuation from unknown ice temperature and chemistry, making assessment of basal conditions from echo strengths difficult.

To address these challenges in interpreting basal properties at glaciologically relevant scales, a new algorithmic approach is applied to measuring the radar scattering function of the bed in terms of the relative contribution of angularly narrow specular energy and isotropically scattered diffuse energy.

This relative specularity content is insensitive to englacial attenuation and can be used to constrain the geometry of the bed down to the centimeter scale.

This approach is applied to an airborne radar sounding survey of Thwaites Glacier, West Antarctica using the information in the along-track scattering function to assess the extent and geometry of water across the catchment and detect the transition of that water from distributed canals to concentrated channels. This information is also used to constrain the morphology of subglacial bedforms and infer that the distribution of deformable sediments and exposed bedrock is similar to deglaciated paleo ice streams that experienced meltwater intensive retreats. Finally, models of radar echo strength and subglacial water routing are compared to estimate a catchment-wide distribution of geothermal flux consistent with rift-associated magma migration and volcanism. These observations of basal conditions provide new context for the past, current, and future evolution of Thwaites Glacier, the West Antarctic Ice Sheet, and their contribution to global sea level.

Table of Contents

Acknowledgments **v**

Abstract **vii**

List of Figures **xi**

List of Tables **xvi**

Chapter 1. Introduction **1**

1.1 Ice sheet contributions to sea level 1

1.2 Basal boundary conditions for subglacial hydrology 6

1.2.1 Subglacial water 6

1.2.2 Subglacial sediments 9

1.2.3 Subglacial geothermal flux 9

1.2.4 Observing subglacial boundary conditions 10

1.3 Airborne radar sounding 11

1.4 Scope of chapters 15

Chapter 2. Subglacial water configuration **18**

2.1 Introduction 19

2.2 Results 22

2.3 Conclusions 27

2.4 Methods 28

2.5 Supporting information 29

2.5.1 Specularity content of radar returns 29

2.5.2 Focusing with different apertures 30

2.5.3 Calculating specularity content 31

2.5.4 Interpreting specularity from a gridded survey 32

Chapter 3. Subglacial water geometry **34**
3.1 Introduction . . . 35
3.2 Specularity content of bed echoes . . . 37
3.3 Roughness of ice/water interfaces . . . 39
3.4 Thickness of subglacial water layers . . . 42
3.5 Length of subglacial water bodies . . . 45
3.6 Width of subglacial water bodies . . . 47
3.7 Conclusions . . . 48

Chapter 4. Deformable sediments and exposed bedrock **49**
4.1 Introduction . . . 50
4.2 Methods . . . 51
4.3 Radar inferred bedforms and lithology . . . 54
4.4 Conclusions . . . 57
4.5 Supporting information . . . 57
4.5.1 Bedform orientation from anisotropic specularity . . . 57
4.5.2 Angularly dependent bed echo specularity . . . 59
4.5.3 Angularly dependent specularity of a corrugated bed . . . 59
4.5.4 Modeled specularity from bathymetry data . . . 61

Chapter 5. Heterogenous geothermal flux **62**
5.1 Introduction . . . 63
5.2 Results . . . 65
5.3 Conclusions . . . 69
5.4 Methods . . . 70
5.4.1 Subglacial water flux and bed echo strengths . . . 70
5.4.2 Geometric spreading losses and englacial attenuation . . . 71
5.4.3 Subglacial water routing . . . 72
5.4.4 Estimated basal melt rates and geothermal flux . . . 74

Chapter 6. Conclusion **76**

Bibliography **85**

Vita **104**

List of Figures

1.1 (a) Range of estimated sea level rise over the next century from ice sheet and climate models (these models do not include the processes or influence of subglacial hydrology) [21]. (b) History of paleo sea level changes (adapted from [105]) with the current rate (solid black line) and maximum modeled rate (dashed black line) (from (a) [21]). 2

1.2 Bed elevation for (a) Antarctica [33] and (b) Greenland [8] showing the regions of the West Antarctic, East Antarctic, and Greenland Ice Sheets grounded below sea level. 3

1.3 (a) Ice sheet surface speed from InSAR (adapted from [91]) and (b) mass loss from satellite gravity [19] for Antarctica and the ASE (black squares). 3

1.4 Model illustrating ice sheet grounding line instability on landward-sloping beds (adapted from [95]). Once the grounding line moves landward of a stable position on the seaward-sloping bed of the outer shelf (seaward solid line in (a)) unstable retreat occurs from an unstable position on the landward-sloping bed (dashed line in (a) and t = 0 in (b)) to the the next stable position (landward solid line in (a)) on a seaward-sloping bed. 4

1.5 (a) Bed topography for the ASE [33] showing the retreat paths to the deep interior for Pine Island Glacier (dashed white line) and Thwaites Glacier (solid white line). (b) The landward sloping bed of Pine Island Glacier is contained by high seaward-sloping topography (adapted from [109]). (c) The landward sloping bed of Thwaites Glacier reaches into the deep interior of the WAIS (adapted from [41]). 5

1.6 (a) Correlation of ice sheet surface lowering, mass loss, and warm ocean temperature [86]. (b) Ice sheet acceleration from the drainage of subglacial lakes [106]. 6

1.7 Illustration of subglacial lakes and water systems across the subsurface of the Antarctic Ice Sheet (adapted from [74]). . . . 7

1.8 (a) Physical model of subglacial canals eroded into sediment [18]. (b) Picture of a concentrated subglacial channel ($\sim$ 1.5 m high) [32]. 7

1.9 Silt unit on the continental shelf of the ASE from paleo Pine Island Glacier. (a) Plan-view of the ASE continental shelf. (b) Particle size distribution of the silt unit [116]. (c) Pb^{210} curve and inferred sedimentation rate for the silt unit (white dot in (a)) (adapted from [116]). (d) Cross-section of the silt unit (white line in (a)) (adapted from [49]). 8

1.10 Retreat across beds with distinct lithology and rheology. (a) Model of future retreat scenarios for Thwaites Glacier for a linear-viscous bed (basal rheology for ice on bedrock) and a plastic bed (basal rheology for ice on deformable sediments) (adapted from [82]). (b) Illustration of retreat for the paleo Pine Island Glacier across bed regions with deformable sediments (brown color added) and exposed bedrock (grey color added) (adapted from [49]). 10

1.11 Radar sounding profile of a subglacial volcano and englacial ash layer in West Antarctica [59]. 11

1.12 Photograph of airborne radar sounding antennas mounted beneath the wings of a survey aircraft [72]. 12

1.13 (a) Radar profiles produced by i) incoherent averaging, ii) coherent summation and incoherent averaging, and iii) SAR focusing [15]. (b) Radar sounding profile of a subglacial lake [16]. . . . 13

1.14 Model demonstrating the potential for erroneously interpreting strong subsurface returns as extant subglacial water [64]. Note that the strongest relative bed echoes do not occur above the areas with basal melt (because of increased attenuation above those warmer areas). 14

2.1 Thwaites Glacier, West Antarctica. (a) The bed elevation of the Thwaites Glacier catchment (black square) in the context of the marine West Antarctic Ice Sheet (b) The bed elevation for only the Thwaites Glacier catchment. (c) The orthogonal 15 km survey grid of the Thwaites Glacier catchment shown in the context of ice-surface speeds above 35 m/yr [91]. The dark and light magenta dots show the locations for the radargrams in Figure 2.4b. 22

2.2 Echo specularity from an anisotropic subglacial water system. (a) The average of the bed echo specularity for orthogonal grid directions shown with the subglacial hydrologic pathways derived from surface and bed elevations [36]. The bed echo specularity for the (b) north-south grid direction and (c) east-west grid direction. 23

2.3 Concentrated channels and distributed canals. Cartoon representations of the subglacial water configuration and radar scattering for: (a) concentrated channels carved into the overlying ice with an approximately semi-cylindrical reflecting interface and (b) distributed canals eroded into the underlying sediment with an approximately planar reflecting interface [112]. 24

2.4 Transition from distributed canals to concentrated canals in Thwaites Glacier. (a) Specularity content in the context of subglacial hydraulic potential (contours) and tributary boundaries (black lines) showing high specularity values in the tributaries and upper trunk. Three major subglacial pathways (light grey lines) and the distributed to concentrated transition (dark grey box) are also shown. (b) Bed echo strength and specularity content for three major subglacial pathways (with distributed to concentrated transition in grey). (c) The width-averaged surface profile, upstream basal melt-water, and basal shear stress. (d) Focused cross-flow radargrams showing broad reflectors consistent with distributed canals (dark magenta dot) upstream of the transition and concentrated channels downstream (light magenta dot), each with about 2100 m of ice cover. 26

3.1 Geometry for the path of a radar return from a point on the ice/bed interface. 37

3.2 Model for the scattering function of (a) a purely specular reflecting interface, (b) a purely diffuse isotropically scattering interface, and (c) an interface that returns both diffuse and specular energy. 38

3.3 Cartoon of the roughness of the ice/water interface RMS_w of a subglacial water layer of finite thickness T. 40

3.4 Reduction in reflected power at nadir as a function of surface roughness described by Equation 3.9 (dashed-line) and Equation 3.11 (solid line). 41

3.5 Specularity of radar bed echoes as a function of the roughness of the ice/water interface. 43

3.6 Specularity content of radar bed echoes as a function of water layer thickness T and conductivity σ_w (a σ_w value of about 0.0002 is typical of pure water, of about 4 is typical of sea water, and about 1 is typical of ground water [84, 25, 94]). 44

3.7 Observation geometry for a subglacial water body with a rectangular reflecting interface. 45

3.8 Specularity content of radar bed echoes as a function of subglacial water body length. 46

3.9 Specularity content of radar bed echoes as a function of observation angel Θ_w and water body width W_w. 48

4.1 Bathymetry and bed topography [7] of the (a) ASE, including the sediment to bedrock transition on the inner continental shelf (solid white line) [49] and the distributed to concentrated subglacial water system transition beneath Thwaites Glacier (dashed white line) [97]. Bathymetry of the (b) exposed bedrock on the inner continental shelf [73] and (c) lineated sedimentary bedforms on the outer continental shelf [42, 5]. 52

4.2 Radar profiles from a gridded airborne survey of (a) the Thwaites Glacier catchment, showing the along flow (b) and across flow (c) bedforms of the downstream region as well as the across-flow (d), oblique-to-flow (e), and along-flow (f) bedforms of the upstream region. 55

4.3 Anisotropy of bedform radar scattering. (a) Axis of symmetry (aligned with black dashes) for anisotropic, low specularity areas in the context of ice flow [93]. Angularly dependent specularity for the downstream (b) and upstream (c) regions of the Thwaites Glacier bed. Analytic specularity response for a sinusoidally corrugated sedimentary bed [100] with crest-to-trough heights, crest-to-crest widths, and surface texture rms-slopes of (i) 150 m, 6 m, and 7.5° (e.g. the ASE continental shelf (Figure 4.1c) [42]), (ii) 300 m, 10 m, and 9° (e.g. Rutford Ice Stream [48]), (iii) 500 m, 20 m, and 10° (e.g. upstream Thwaites Glacier (Figure 4.2d). Modeled specularity for bathymetry of (d) exposed bedrock (Figure 4.1b) and (e) lineated sediments (Figure 1c) on the ASE continental shelf. 56

5.1 (a) Bed topography of the West Antarctic Ice Sheet and Amundsen Sea Embayment [33]. (b) Subglacial hydrologic potential [53] for a distributed water system in the upstream region of the Thwaites Glacier catchment (black boundary). (c) Collection of subglacial water routing models that best fit the observed radar bed-echo strength distribution (Figure 5.2a), where the darkness of grayscale cells is the number of models (out of 50) for which these cells drain at least 10 others upstream. 65

5.2 (a) Mean estimate of observed relative radar bed-echo strengths for the Thwaites Glacier catchment (black boundary) corrected for geometric spreading losses. (b) Range of estimates of corrected relative bed-echo strengths. Minor banding is due to variations in aircraft height above the ice surface combined with the different geometric loss terms. Bed topography [33] contour interval for Antarctica is 180 m. 66

5.3 Minimum geothermal flux and basal melt values required to reproduce the observed relative bed-echo strengths (Figure 2a) with subglacial water routing models [53, 40] (Figure 1c) using the total melt water from an ice sheet model for the upstream portion of the Thwaites Glacier catchment [46]. The minumum average inferred flux is $\sim 114 \pm 10$ mW/m^2. High flux areas exceed 200 mW/m^2. (a) The Mount Takahe volcano. (b) WAIS Divide ice core drilling site. High melt areas (c) in the westernmost tributary, (d) adjacent to the Crary mountains, and (e) in the upper portion of the central tributaries [10]. Triangles show areas where radar-inferred melt anomalies exceed those generated by ice dynamics (friction and advection) [46] and inferred geothermal flux exceeds 150 mW/m^2 (dark magenta) and 200 mW/m^2 (light magenta). Bed topography [33] contour interval for Antarctica is 180 m. 68

6.1 Cartoon illustrating the evolution of the hydrologic basal boundary conditions for Thwaites Glacier. (a) Paleo Thwaites Glacier, grounded on the outer continental shelf and underlain by a pervasive distributed water network, which is transporting and storing silt from the subglacial till. (b) Paleo and contemporary Thwaites Glacier grounded over a region of exposed bedrock on the inner continental shelf. The subglacial water system transitions from distributed canals upstream to concentrated channels downstream, which are eroding silt stored in bedrock basins. (c) Thwaites Glacier, once it reaches the upstream portion of the catchment and is grounded on deformable sediments with a distributed water system. In each configuration, the subglacial water system is being fed by melt from elevated and variable geothermal flux due to rift-associated magmatic migration and volcanism upstream. 80

List of Tables

1.1 University of Texas HiCaRS Radar System 12

Chapter 1

Introduction

This dissertation is focused on using the information in radar sounding data to observe boundary conditions relevant to understanding the impact of subglacial hydrology on the stability of Thwaites Glacier and the West Antarctica Ice Sheet.

1.1 Ice sheet contributions to sea level

The rate and amount of sea level rise is one of the most tangible and societally impacting effects of a changing climate [104]. One of the greatest sources of uncertainty in predictions of sea level over policy relevant time scales is the contribution of continental ice sheets (Figure 1.1a) [21]. This is due, in large part, to unknown physics, processes, and conditions that govern ice sheet behavior and evolution, particularly during periods of unstable retreat. The geologic record of past sea level (Figure 1.1b) shows periods of rapid sea level rises with rates as high as $\sim$2 cm/yr (compared to the current rate of $\sim$3 mm/yr) [105] and neither current observations nor modeling can definitively exclude the possibility of future rates on the same order [104].

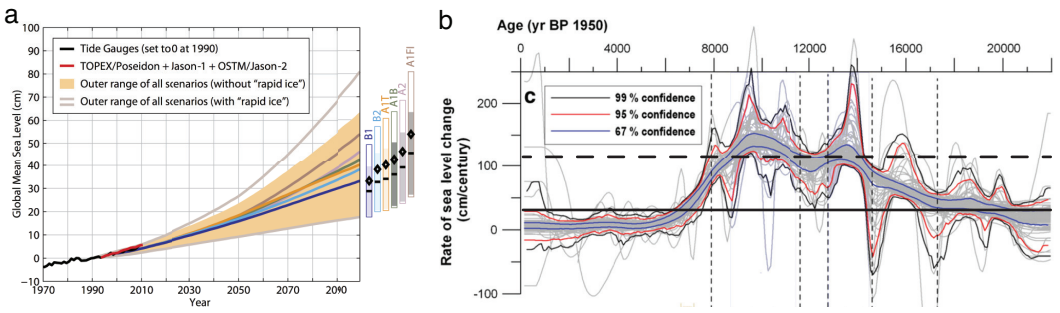

Figure 1.1: (a) Range of estimated sea level rise over the next century from ice sheet and climate models (these models do not include the processes or influence of subglacial hydrology) [21]. (b) History of paleo sea level changes (adapted from [105]) with the current rate (solid black line) and maximum modeled rate (dashed black line) (from (a) [21]).

One of the critical processes in assessing the potential sea level contribution of continental ice sheets is the *Marine Ice Sheet Instability*, which suggests that the portions of ice sheets grounded below sea level (Figure 1.2) may be susceptible to rapid unstable retreat [114]. Ice sheet sectors that are grounded below sea level include some of the fastest moving (Figure 1.3a) and most rapidly changing glaciers (Figure 1.3b) on earth [91, 19]. The sector with the greatest recent observed acceleration and mass loss is the Amundsen Sea Embayment (ASE) of the West Antarctic Ice Sheet (WAIS) (Figure 1.3). A critical mechanism governing the potential for unstable retreat is the reduced capacity for marine ice sheets on landward-sloping beds to achieve stable grounding configurations. Once a retreat starts in a landward-sloping area it has the potential to unstably retreat until it reaches a seaward-sloping portion of the bed (Figure 1.4) [95].

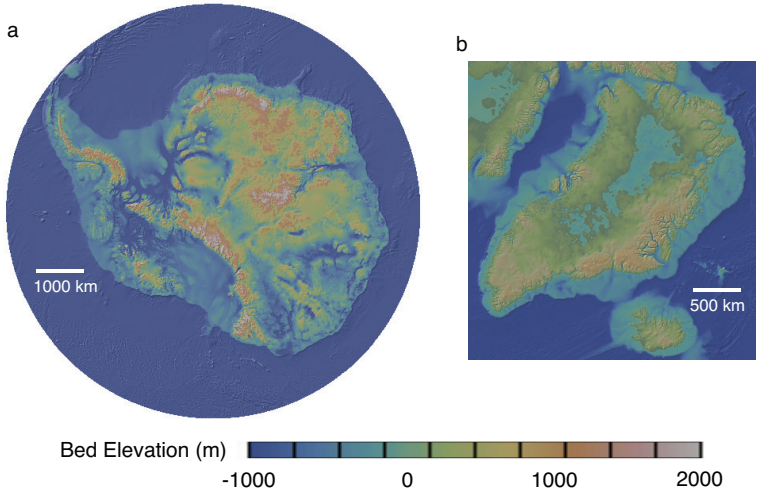

Figure 1.2: Bed elevation for (a) Antarctica [33] and (b) Greenland [8] showing the regions of the West Antarctic, East Antarctic, and Greenland Ice Sheets grounded below sea level.

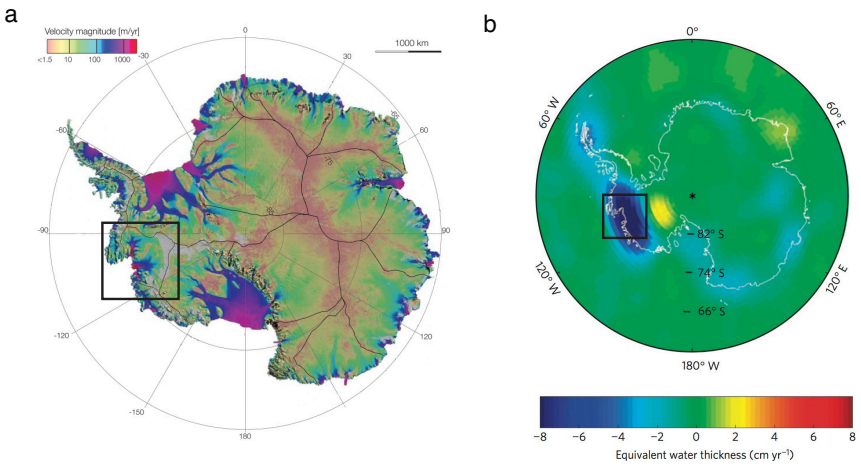

Figure 1.3: (a) Ice sheet surface speed from InSAR (adapted from [91]) and (b) mass loss from satellite gravity [19] for Antarctica and the ASE (black squares).

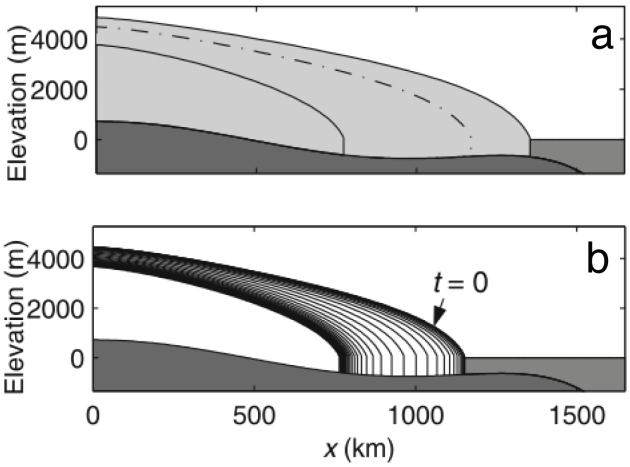

Figure 1.4: Model illustrating ice sheet grounding line instability on landward-sloping beds (adapted from [95]). Once the grounding line moves landward of a stable position on the seaward-sloping bed of the outer shelf (seaward solid line in (a)) unstable retreat occurs from an unstable position on the landward-sloping bed (dashed line in (a) and t = 0 in (b)) to the the next stable position (landward solid line in (a)) on a seaward-sloping bed.

The Amundsen Sea Embayment (ASE) contains two of the most rapidly changing glaciers in the world (Figure 1.3, Figure 1.5). Pine Island Glacier has a landward sloping bed, but its catchment is contained by high topography (Figure 1.5b). Thwaites Glacier has a landward-sloping bed that reaches the deep interior of the ice sheet, so that a retreat started in its trunk has the potential to spread to the rest of the WAIS (Figure 1.5c) [41, 109].

Warm ocean water has been observed on the inner shelf of the ASE (Figure 1.6a) and is thought to contribute to the observed acceleration of the Thwaites and Pine Island Glaciers through enhanced melting near the grounding zone [86]. Although the ocean is likely a significant forcing in the

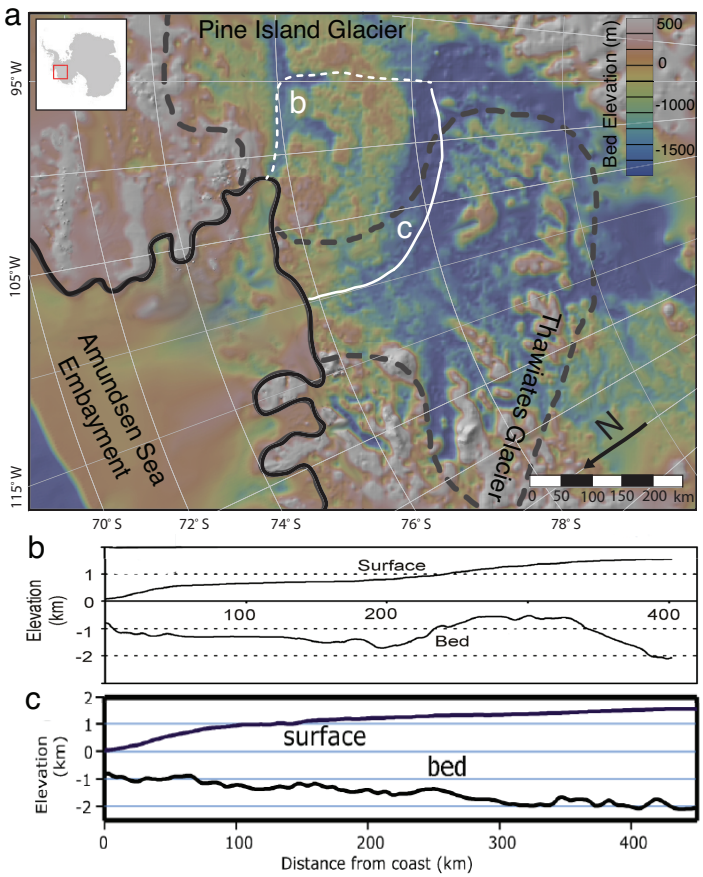

Figure 1.5: (a) Bed topography for the ASE [33] showing the retreat paths to the deep interior for Pine Island Glacier (dashed white line) and Thwaites Glacier (solid white line). (b) The landward sloping bed of Pine Island Glacier is contained by high seaward-sloping topography (adapted from [109]). (c) The landward sloping bed of Thwaites Glacier reaches into the deep interior of the WAIS (adapted from [41]).

recent observed changes, the basal boundary conditions of Thwaites Glacier will also play a critical role in determining the pacing, character, and extent of its eventual retreat [82, 113, 62, 20, 106].

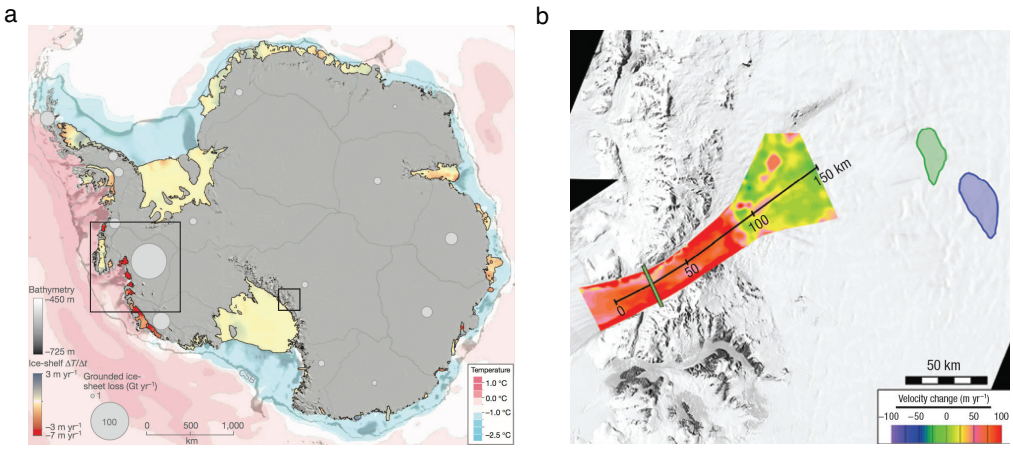

Figure 1.6: (a) Correlation of ice sheet surface lowering, mass loss, and warm ocean temperature [86]. (b) Ice sheet acceleration from the drainage of subglacial lakes [106].

1.2 Basal boundary conditions for subglacial hydrology

1.2.1 Subglacial water

Like warm ocean water, subglacial water systems have been observed to accelerate large outlet glaciers [106] (Figure 1.6b). Subglacial water has also been observed to modulate the fast flow or stagnation of ice streams and mountain glaciers [2, 32]. Dynamic and diverse subglacial water systems across the subsurface of East and West Antarctica (Figure 1.7) [101] have been variously observed and theorized to take on a range of configurations (i.e., saturated tills, linked cavities, layers, lakes) [32].

Despite this diversity, there are only two categories of water system configurations that govern the effect of subglacial water on ice flow [24]. The first category is distributed subglacial water, in which effective pressure, basal

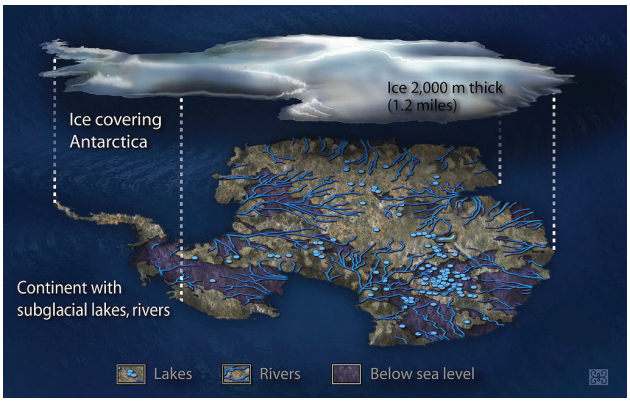

Figure 1.7: Illustration of subglacial lakes and water systems across the subsurface of the Antarctic Ice Sheet (adapted from [74]).

lubrication, and ice flow increases with increasing water flux (e.g. distributed subglacial canals eroded into subglacial sediments (Figure 1.8a) [112]). The second category is concentrated subglacial water, in which effective pressure, basal lubrication, and ice flow decreases with increasing water flux (e.g. concentrated subglacial channels eroded into the overlying ice (Figure 1.8b) [32]).

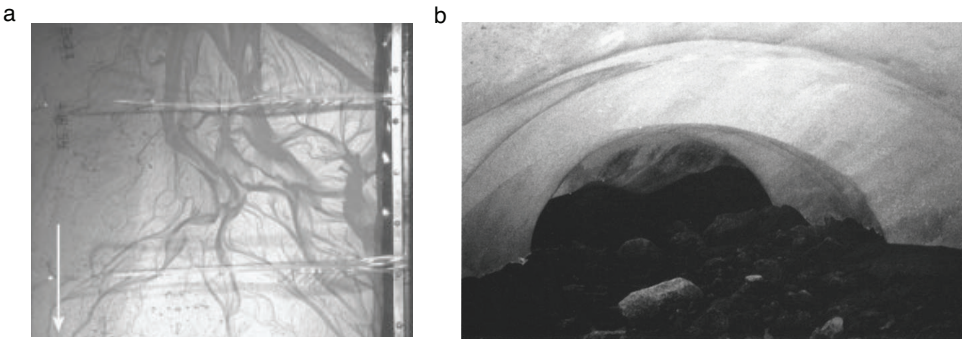

Figure 1.8: (a) Physical model of subglacial canals eroded into sediment [18]. (b) Picture of a concentrated subglacial channel ($\sim$ 1.5 m high) [32].

The geologic, morphologic, and sedimentary records of paleo ice sheets also provide insight into the configurations, settings, and impacts of past subglacial water systems. For example, there is evidence that concentrated subglacial water once flowed through a network of channels beneath paleo Pine Island Glacier [73], leaving a modern (Figure 1.9c) plumite deposit of finely sorted silt on the deglaciated shelf of the ASE (Figure 1.9)[116].

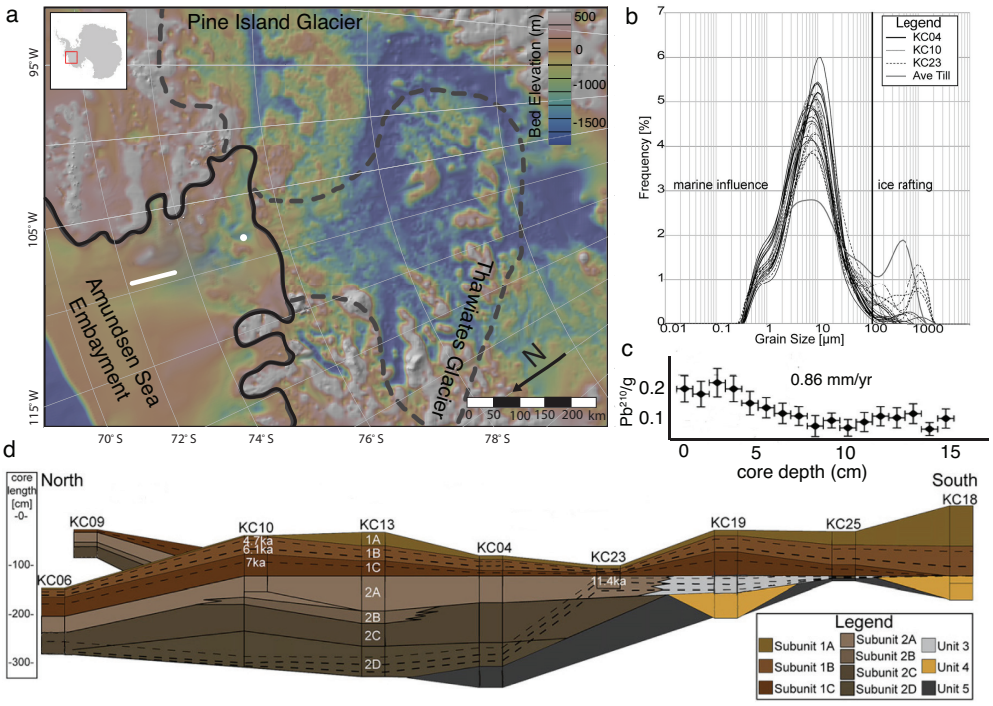

Figure 1.9: Silt unit on the continental shelf of the ASE from paleo Pine Island Glacier. (a) Plan-view of the ASE continental shelf. (b) Particle size distribution of the silt unit [116]. (c) Pb^{210} curve and inferred sedimentation rate for the silt unit (white dot in (a)) (adapted from [116]). (d) Cross-section of the silt unit (white line in (a)) (adapted from [49]).

1.2.2 Subglacial sediments

The distribution of deformable sediments and exposed bedrock beneath an ice sheet determines the bed rheology and can control ice sheet evolution, stability, and retreat [82, 20] (Figure 1.10a). Basal lithology and rheology also control ice surface slopes, affecting the subglacial hydrologic potential [112] and the possibility for retreats initiated or facilitated by subglacial water. The importance of basal lithology to ice sheet stability is also evident in paleo ice stream records, which provide morphologic and geologic evidence of retreats with distinct pacing and character across regions of deformable sediments and regions of exposed bedrock (Figure 1.10b) [49].

1.2.3 Subglacial geothermal flux

The acceleration of ice flow by subglacial water is determined by the existence and configuration of concentrated and distributed subglacial water across the ice sheet bed as well as the time-variable supply of subglacial water into these systems [96]. One source of large and variable water supply is the drainage of subglacial lakes (Figure 1.6b) [106]. Another is geothermally generated meltwater volumes associated with magma migration [59] and subglacial volcanism [110, 12, 15, 14]. Thwaites Glacier lies within the West Antarctic Rift System (WARS), a region with poorly constrained geothermal flux [66, 99]. However, high geothermal flux values [22] and active subglacial volcanism nearby (Figure 1.11) [59] suggest that elevated and spatially variable geothermal flux is an influential boundary condition for Thwaites Glacier.

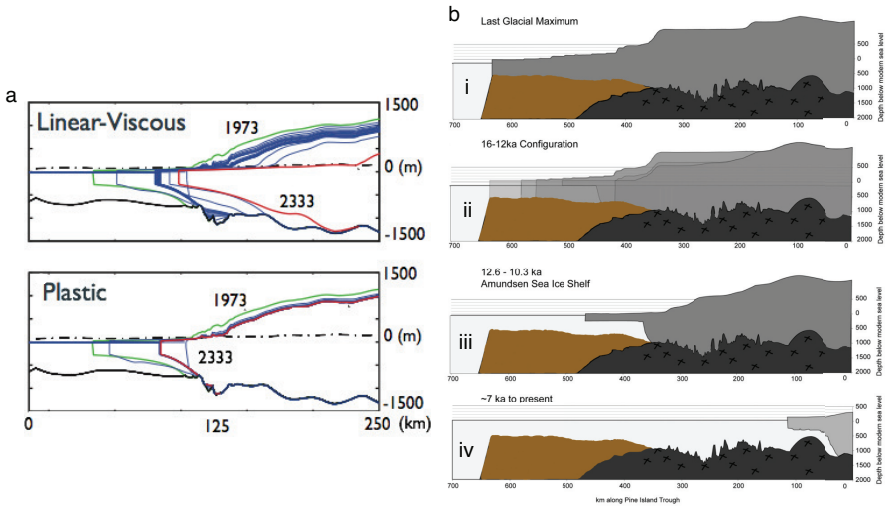

Figure 1.10: Retreat across beds with distinct lithology and rheology. (a) Model of future retreat scenarios for Thwaites Glacier for a linear-viscous bed and a plastic bed (adapted from [82]). (b) Illustration of retreat for the paleo Pine Island Glacier across bed regions with deformable sediments (brown color added) and exposed bedrock (grey color added) (adapted from [49]).

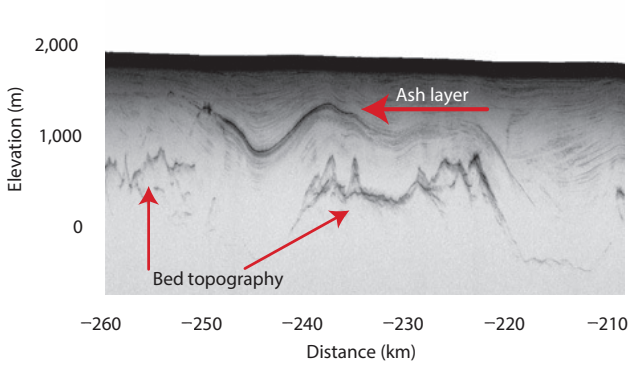

Figure 1.11: Radar sounding profile of a subglacial volcano and englacial ash layer in West Antarctica [59].

1.2.4 Observing subglacial boundary conditions

Assessing the the potential for the subglacial water system of Thwaites Glacier to trigger or facilitate an unstable retreat, requires observing:

1. The spatial distribution of subglacial water across the catchment
2. The physical configuration and hydrologic dynamic state of that water
3. The lithologic setting of the water system and ice sheet bed
4. How the bed configuration compares to paleo ice streams
5. The distribution and variability of geothermal flux and basal melt

1.3 Airborne radar sounding

Since the bed lies beneath kilometers of ice and requires characterization of meter-scale properties across an entire glacier catchment, airborne radar sounding is the only practical tool for observationally constraining these dynamically critical boundary conditions.

The airborne radar sounding data used in this work was collected by the University of Texas Institute for Geophysics High Capability Radar Sounder (HiCaRS) [37, 69, 84]. This radar transmits linear chirped radar pulses (Table 1.1) through an array of two flat-plate dipole antennas mounted beneath the wings of an airplane [83] (Figure 1.12). Radar pulses are transmitted through the air/ice interface (where they are refracted) and reflected from englacial

(e.g. layers) and subglacial (e.g. bedforms, subglacial water) interfaces with contrasting electrical properties (dielectric constant and conductivity), then transmitted (and refracted) back through the ice/air interface and collected by the same airborne antenna array [84].

Figure 1.12: Photograph of airborne radar sounding antennas mounted beneath the wings of a survey aircraft [72].

Table 1.1: University of Texas HiCaRS Radar System

Center Frequency	Bandwidth	Pulse Repetition Frequency	Transmit Power
60 MHz	15 MHz	6.4 kHz	8 kW

From theses pulses, radar images are produced by a combination of coherent summation, incoherent averaging, focusing, and range migration [87, 57, 55, 83, 38, 80, 118]. This focusing uses the phase history of the recorded radar data to resolve Doppler frequencies and map the received energy to the correct range and azimuth [83, 88]. By focusing with larger apertures, the energy is mapped back for greater scattering angles and more steeply sloped specular interfaces; increasing the azimuth gain, reducing clutter, improving

the resolved morphology, and making interpretation of englacial and subglacial features easier (especially in areas with high clutter) [83] (Figure 1.13a).

In processed radargrams, subglacial water bodies are typically interpreted as flat and bright features (Figure 1.13b), which are bright because of their increased dielectric contrast with the ice (compared the contrast between the ice and bed) and which are flat because of subglacial melt-freeze processes that tend to produce flat interfaces for water bodies in hydrostatic equilibrium with the ice sheet [16, 79]. The limitation of the brightness criteria is that echoes can be strong either because of the geometric and material properties of the basal interface (i.e. the presence of subglacial water) or because of differential englacial attenuation (a function of ice temperature and chemistry [63]), which can lead to erroneous interpretation of high echo strengths as extant basal water [64] (Figure 1.14).

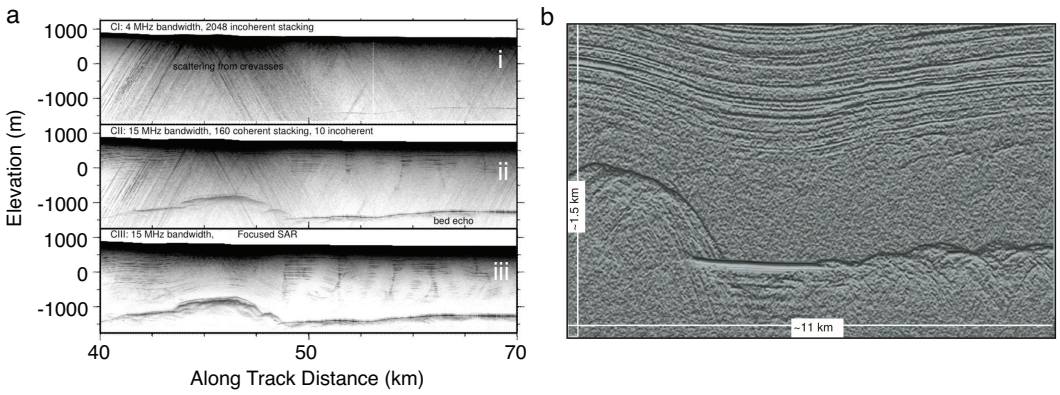

Figure 1.13: (a) Radar profiles produced by i) incoherent averaging, ii) coherent summation and incoherent averaging, and iii) SAR focusing [15]. (b) Radar sounding profile of a subglacial lake [16].

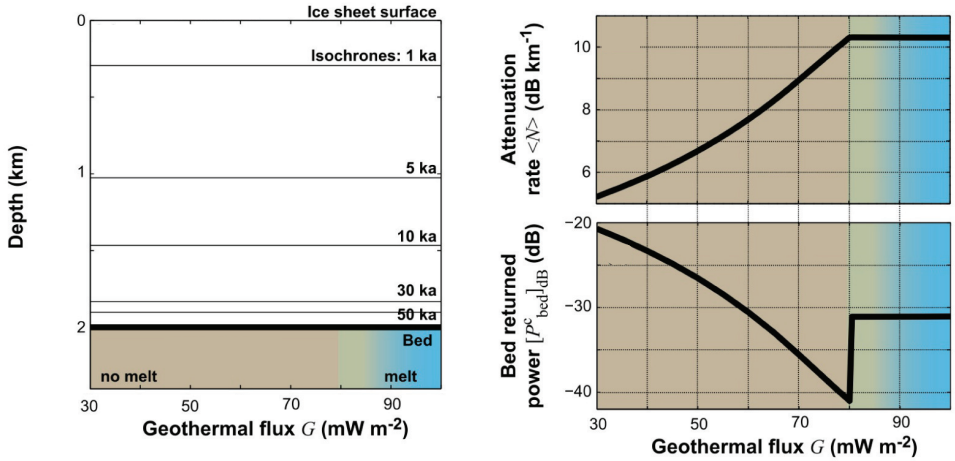

Figure 1.14: Model demonstrating the potential for erroneously interpreting strong subsurface returns as extant subglacial water [64]. Note that the strongest relative bed echoes do not occur above the areas with basal melt (because of increased attenuation above those warmer areas).

The limitation of the flatness criteria is that it requires water bodies to span enough azimuth resolution cells to be interpretable as flat, however many subglacial water bodies have dimensions at, near, or below the along track resolution of radar sounding systems [32]. There is a similar challenge when using radar-resolved bedforms to infer the distribution of deformable sediments and exposed bedrock, which have morphological signatures that are also often near or below radar resolution [58].

The use of radar sounding data to constrain melt rates has been limited to the interpretation of bed echo strengths [84, 14] to infer basal water (which is subject to the same limitations discussed above) or radar layer drawdown to infer melted ice loss at the bed [30]. However, the interpretation of layer draw-

down is limited by the existence, persistence, and interpretability of layers in radar sounding profiles and the requirement of well constrained accumulation rates [30].

Amid these challenges, the work in this dissertation seeks to provide a foundation for placing observational constraints on and providing deeper understanding of these critical basal boundary condition for Thwaites Glacier and its subglacial water system using underexploited information in radar bed echoes.

1.4 Scope of chapters

Chapter 1 is an introductory chapter meant to provide the background necessary to understand Chapters 2, 3, 4, and 5, which were written as stand-alone papers and consequently have some redundant introductory material.

Chapter 2 focuses on using the specularity of radar bed echoes to detect a transition in the subglacial water system from a network of distributed canals in the upstream portion of the catchment to a network of concentrated channels in the downstream portion. A version of this chapter was published in the *Proceedings of the National Academies of Science of the United States of America* under the title "Evidence for a water system transition beneath Thwaites Glacier, West Antarctica" with co-authors D. D. Blankenship and D. A. Young [97]. Both of whom provided insight and feedback on the analysis and manuscript writing.

Chapter 3 focuses on estimating the geometry of the distributed subglacial water bodies in the upstream portion of the Thwaites Glacier catchment using a series of simple radar scattering, attenuation, and cross section models to show that the water bodies have ice/water interface roughnesses of less than about 15 cm, thicknesses of greater than about 5 cm, lengths of greater than about 15 m, and widths between about 0.5 and 5 m. A version of this chapter is in review with *IEEE Geoscience and Remote Sensing Letters* under the title "Estimating subglacial water geometry using radar bed echo specularity: application to Thwaites Glacier, West Antarctica" with co-authors D. D. Blankenship, R. K. Raney, and C. Grima. All of whom provided insight and feedback on the analysis and manuscript writing.

Chapter 4 uses the variation of the bed echo specularity as a function of observation angle to show that the downstream portion of Thwaites Glacier is grounded on a region of exposed bedrock and that the upstream portion of the catchment is underlain by a layer of deformable sediments with ice flow aligned lineated bed forms. This configuration is similar to that of nearby paleo Pine Island Glacier when it experienced a relatively rapid, backstepping, meltwater intensive retreat across the inner continental shelf [116]. A version of this chapter is in review with *Geophysical Research Letters* under the title "Airborne radar sounding reveals pervasive deformable sediments with significant bedrock buttressing beneath Thwaites Glacier, West Antarctica" with co-authors D. D. Blankenship, D. A. Young, A. E. Witus, and J. B. Anderson. D.D. Blankenship and D. A. Young provided insight and feedback on the data

analysis and manuscript writing. A. E. Witus and J. B. Anderson provided provided insight, feedback, and special expertise on integration observations of paleo ice stream remnants on the continental shelf.

Chapter 5 uses a combination of bed echo strength and subglacial water routing models to produced a radar-based map of the spatial distribution of geothermal flux across the Thwaites Glacier catchment. It estimates a catchment-wide average flux of $\sim$114 mW/m^2 with areas of high flux exceeding 200 mW/m^2 and consistent with rift-associated magma migration and volcanism. A version of this chapter is in review with the *Proceedings of the National Academies of Science of the United States of America* under the title "Evidence for Elevated and spatially variable geothermal flux beneath the West Antarctic Ice Sheet" with co-authors D. D. Blankenship, D. A. Young, and E. Quartini. All of whom provided insight and feedback on the analysis and manuscript writing.

Chapter 6 is a short conclusion chapter that integrates the findings of Chapters 2, 3, 4, and 5 to provide new insight into the hydrologic evolution of Thwaites Glacier.

Chapter 2

Subglacial water configuration

Thwaites Glacier is one of the largest, most rapidly changing glaciers on earth and its landward sloping bed reaches the interior of the marine WAIS, which impounds enough ice to yield meters of sea level rise. Marine ice sheets with landward-sloping beds have a potentially unstable configuration in which acceleration can initiate or modulate grounding line retreat and ice loss. Subglacial water has been observed and theorized to accelerate the flow of overlying ice dependent on whether it is hydrologically distributed or concentrated. However, the subglacial water systems of Thwaites Glacier and their control on ice flow have not been characterized by geophysical analysis. The only practical means of observing these water systems is airborne ice penetrating radar, but existing radar analysis approaches cannot discriminate between their dynamically critical states. I use the angular distribution of energy in radar bed echoes to characterize both the extent and hydrologic state of subglacial water systems across Thwaites Glacier. I validate this approach with radar imaging, showing that substantial water volumes are ponding in a system of

A version of this chapter was published in the *Proceedings of the National Academies of Science of the United States of America* under the title "Evidence for a water system transition beneath Thwaites Glacier, West Antarctica" with co-authors D. D. Blankenship and D. A. Young [97].

distributed canals upstream of a bedrock ridge that is breached and bordered by a system of concentrated channels. The transition between these systems occurs with increasing surface slope, melt water flux, and basal shear stress. This indicates a feedback between the subglacial water system and overlying ice dynamics, which raises the possibility that subglacial water could trigger or facilitate a grounding line retreat in Thwaites Glacier capable of spreading into the interior of the WAIS.

2.1 Introduction

Thwaites Glacier is an outlet glacier in the ASE (Figure 2.1), the most rapidly changing sector of the WAIS [9, 95, 114] and a leading component of deglaciation scenarios [19, 85, 91]. As such, the future stability of Thwaites Glacier is a significant factor in sea-level projections. Although subglacial water has been observed to cause significant acceleration in large Antarctic outlet glaciers [106], the potential for a similar (possibly destabilizing) subglacial-water-driven acceleration in Thwaites Glacier has not been geophysically assessed. Subglacial water systems have a diverse range of configurations [32] including lakes [117], sheets [24], canals [112], channels [112], and saturated tills [1], however, their control on ice flow is principally determined by whether the water is hydrologically *distributed* or *concentrated* [24]. Distributed water systems are inefficient at drainage and increase basal lubrication with increased water flux, whereas concentrated water systems are efficient at drainage and do not increase basal lubrication [24]. Therefore, the sensitivity of ice flow

acceleration and grounding line stability for Thwaites Glacier will depend on the existence of these two kinds of water systems beneath it.

Airborne sounding with ice penetrating radar, as applied in this dissertation, has the unique potential to provide both catchment-scale detection of water extent and meter-scale characterization of the geometrically expressed hydrologic state. Radar sounding is a long-established technique for acquiring ice thickness profiles and has been used to detect large subglacial water bodies as flat and bright surfaces in radargrams [79, 16]. Subglacial water produces stronger echoes than grounded bed because it has a stronger dielectric contrast with the ice; however, echo strength based classifications are subject to ambiguities from temperature and chemical variations [63] within the overlying ice, which can lead to erroneous identification of water at the bed [64] and are insufficient to classify the dynamic state of detected water bodies.

Classification of the dynamic state of subglacial water bodies is enabled by measurement of the angular distribution of the returned energy, a much more powerful method than simple elementary detection. Properties of the angular distribution can be used to constrain the meter-scale geometry, orientation, and hydrologic state of basal water systems.

Hydrologically distributed water systems are in pressure equilibrium with the overlying ice and their melt-freeze processes tend to produce planar reflecting interfaces [78]. Concentrated water systems, by contrast, are not in pressure equilibrium and their water flow can melt channels into the ice with curved reflecting interfaces [112]. This difference in reflecting interface

geometry produces distinct radar scattering signatures that can be used as an indicator of the dynamic state of water systems. In this work, I apply range-migrated synthetic aperture focusing [83] to radar sounding data and quantify the angular distribution of returned energy in terms of a measure I call the specularity content of the bed echo. Specular interfaces produce sharp mirror-like reflections and diffuse interfaces scatter energy uniformly in all directions [71]. Actual surfaces include both specular and diffuse components in their returned energy and I define the specularity content of an interface to be the portion of the returned energy that is contributed by the specular component.

To calculate the specularity content, I compare the focused echo strengths produced using different along-track apertures and determine what portion of the returned energy is contributed by specular reflection. Notably, specularity content only measures the angular distribution of energy in radar returns and is therefore insensitive to attenuation uncertainty from poorly constrained ice temperature and chemistry [63, 64].

The Thwaites Glacier catchment is the location of the most extensive coherent, gridded, airborne radar sounding survey in West Antarctica [41], with ice penetrating radar data collected on a 15 km x 15 km grid, using the 60 MHz HiCARS radar sounder [83] (Figure 2.1c). In this study, I performed range-migrated SAR focusing [83] on over 40,000 line-km of coherent radar sounding profiles to produce two sets of radargrams focused over along-track apertures of 700 m and 2 km, making it possible to calculate the specularity content of bed echoes for the entire catchment.

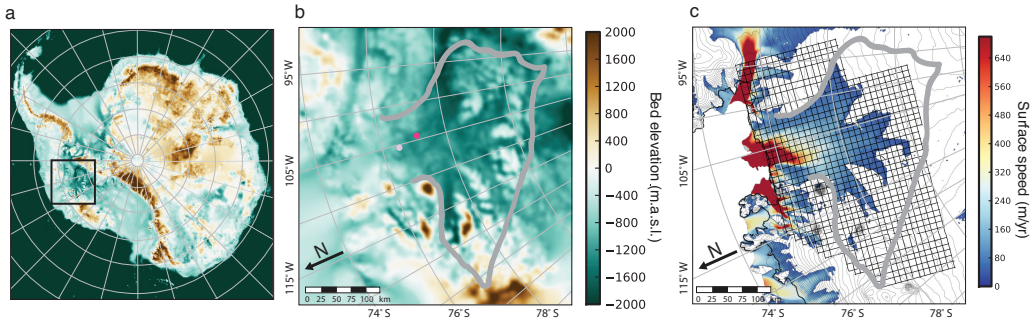

Figure 2.1: Thwaites Glacier, West Antarctica. (a) The bed elevation of the Thwaites Glacier catchment (black square) in the context of the marine West Antarctic Ice Sheet (b) The bed elevation for only the Thwaites Glacier catchment. (c) The orthogonal 15 km survey grid of the Thwaites Glacier catchment shown in the context of ice-surface speeds above 35 m/yr [91]. The dark and light magenta dots show the locations for the radargrams in Figure 2.4b.

2.2 Results

The results show high specularity values in the upstream portion of the catchment that are localized and oriented along modeled hydrologic pathways (Figure 2.2a), indicating flat distributed water bodies in equilibrium with the overlying ice. The orthogonal grid configuration for the survey (Figure 2.1c) also makes it possible to examine each direction of the survey independently, showing that the bed echo specularity is highly anisotropic (Figure 2.2b,c). These results indicate that the subglacial water system is itself anisotropic; restricting the possible configurations of subglacial water to either *distributed canals* [32, 112] or *concentrated channels* [32, 112] (Figure 2.3). Distributed canal systems are composed of networks of flat subglacial water bodies, tens of meters across, which are eroded into sediment at the ice-bed interface and

increase basal lubrication with increased water flux. Concentrated channel systems are composed of networks of roughly semi-cylindrical subglacial water bodies, a few meters across, that are carved upward into the ice. Such channels have negligible impact on basal lubrication [112].

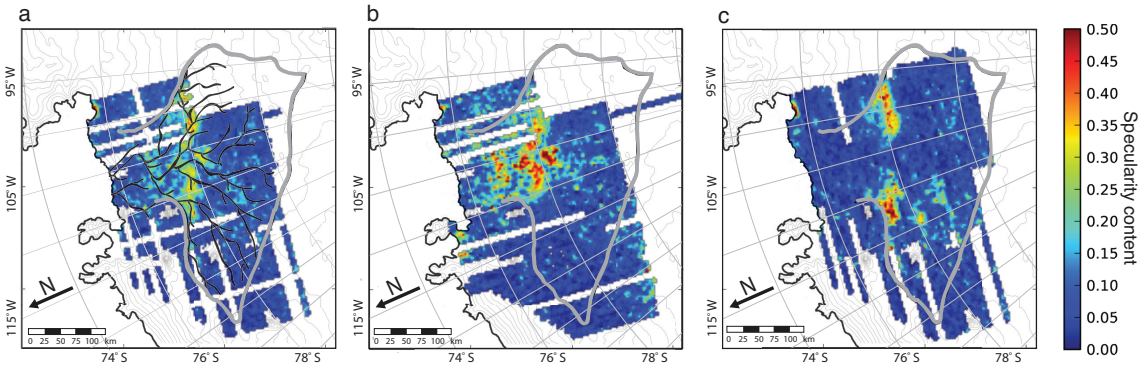

Figure 2.2: Echo specularity from an anisotropic subglacial water system. (a) The average of the bed echo specularity for orthogonal grid directions shown with the subglacial hydrologic pathways derived from surface and bed elevations [36]. The bed echo specularity for the (b) north-south grid direction and (c) east-west grid direction.

The specularity content of bed echoes for Thwaites Glacier (Figure 2.4a) shows high specularity values under the major tributaries and the upstream portion of the trunk. This indicates substantial volumes of water ponding in distributed canals, which increases in area as it approaches a bedrock ridge (visible in Figure 2.1b). Notably, a drop in specularity is evident downstream of the ridge, which could be the result of either of two phenomena: 1) the water system is trapped upstream of the ridge and water is not continuing downstream in sufficient quantities to be detected; or 2) the downstream water

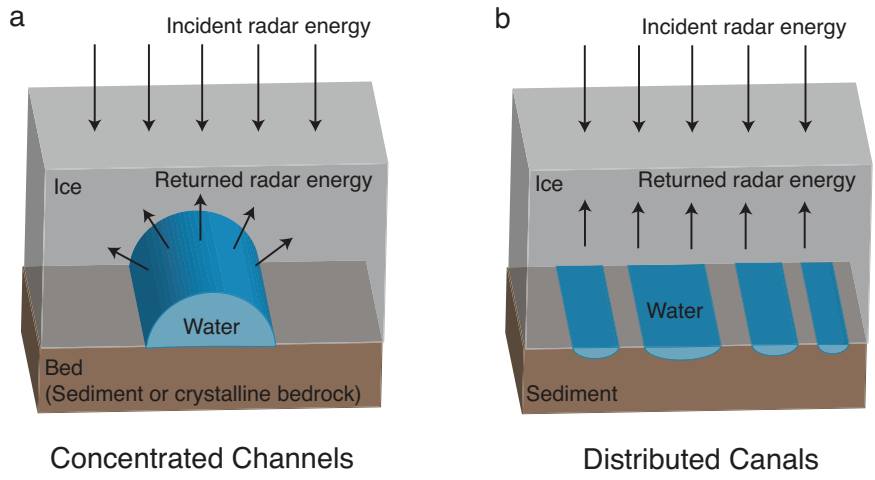

Figure 2.3: Concentrated channels and distributed canals. Cartoon representations of the subglacial water configuration and radar scattering for: (a) concentrated channels carved into the overlying ice with an approximately semi-cylindrical reflecting interface and (b) distributed canals eroded into the underlying sediment with an approximately planar reflecting interface [112].

system has a different configuration that does not have a flat specular surface (e.g. concentrated channels). Distributed subglacial canals and concentrated subglacial channels have distinct morphologies and radar scattering signatures (Figure 2.3). These indicate that a transition from distributed canals to concentrated channels should produce a significant decrease in specularity accompanying a comparatively high relative echo strength [50]. The relative echo strength and specularity content for three major subglacial hydrologic pathways (Figure 2.4b) show that in the upstream region, specularity and relative echo strength do track one another closely and that in the downstream region, specularity does fall as the bed echo strength remains high, matching the ex-

pected response for a canal to channel transition with significant quantities of water continuing to flow past the ridge to the grounding line in a concentrated network. This interpretation is supported by cross-flow focused radargrams (Figure 2.4d) that show broad flat reflectors (consistent with a network of distributed canals) underlie the region upstream of the transition, with bright returns coming from distinct scatters downstream of the transition (consistent with a network of concentrated channels). The transition from a distributed to a concentrated water system occurs with increasing surface slope and basal water flux (Figure 2.4c), which are the conditions under which such a transition is predicted by theoretical studies of the regimes of stability for distributed canals and concentrated channels [112]. The transition is also accompanied by an increase in basal shear stress [46], which is consistent with the theoretical expectations for the impact of such a transition on ice flow, with distributed canal systems reducing basal drag and concentrated channel systems having little or no effect [24].

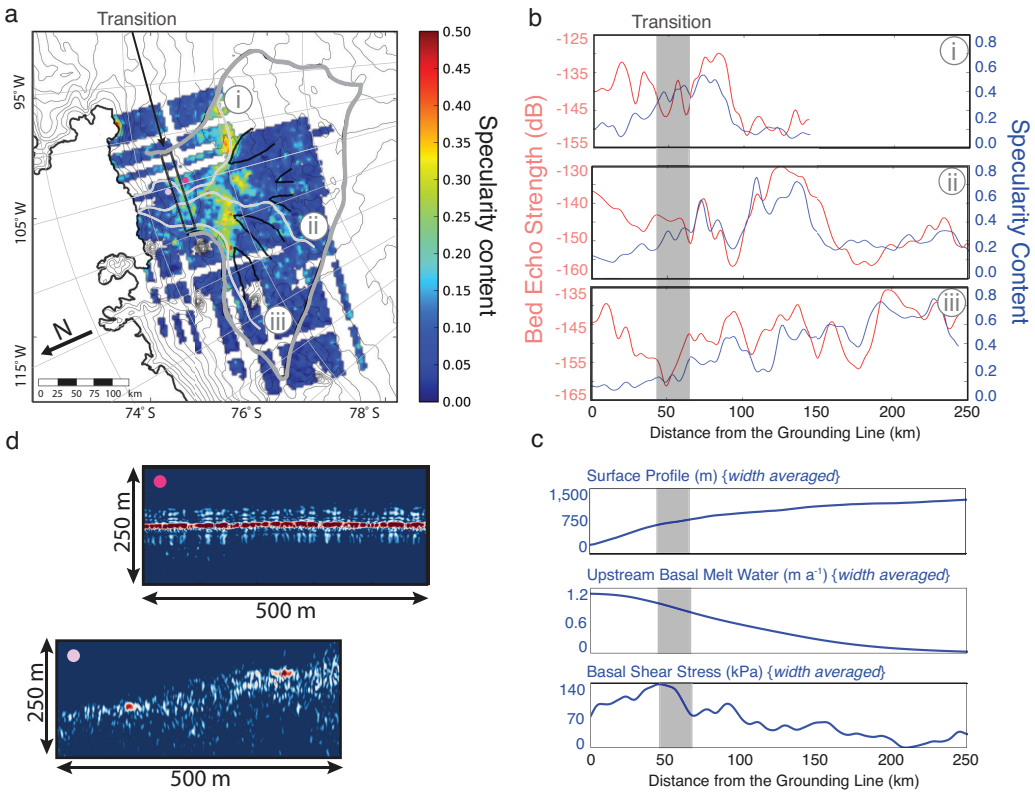

Figure 2.4: Transition from distributed canals to concentrated canals in Thwaites Glacier. (a) Specularity content in the context of subglacial hydraulic potential (contours) and tributary boundaries (black lines) showing high specularity values in the tributaries and upper trunk. Three major subglacial pathways (light grey lines) and the distributed to concentrated transition (dark grey box) are also shown. (b) Bed echo strength and specularity content for three major subglacial pathways (with distributed to concentrated transition in grey). (c) The width-averaged surface profile, upstream basal melt-water, and basal shear stress. (d) Focused cross-flow radargrams showing broad reflectors consistent with distributed canals (dark magenta dot) upstream of the transition and concentrated channels downstream (light magenta dot), each with about 2100 m of ice cover.

2.3 Conclusions

These results provide an attenuation-independent, catchment-wide characterization of the configuration and hydrologic state of the Thwaites Glacier subglacial water system. The system consists of a distributed network of canals ponding behind a bedrock ridge and feeding a system of concentrated channels downstream. Although the concentrated portion of the water system could occupy deeply incised channels like those observed on the deglaciated inner shelf [73], I do not observe deep water-filled basins, which are hypothesized as sources of melt-water floods capable of eroding those channels [73, 4]. The transition from a distributed to a concentrated water system occurs with increasing surface slope, water flux, and basal shear stress, providing observational evidence for the theorized control of the ice surface on the configuration of subglacial water as well as the control of the subglacial water on ice flow. The effect of this direct feedback, like the effect of subglacial sedimentation processes [3], is likely to be temporary stabilization of the Thwaites grounding-line through increased downstream basal traction until external forcing is strong enough to overcome that stabilization and produce a rapid retreat. This particular process and the general feedback between ice flow and subglacial water raises the possibility that subglacial hydrology could play a large, even dominant, role in the evolution, stability, and potential retreat of Thwaites Glacier and the WAIS.

2.4 Methods

The radar data over Thwaites Glacier were collected [41] using a coherent ice penetrating radar system [41] with a center frequency of 60 MHz and a 15 MHz bandwidth. I used coherent, range-migrated, synthetic aperture radar focusing that accounts for refraction at the air/ice interface to produce radargrams for two apertures of approximately 700 m and 2 km. I determine the specularity content by comparing the focused energy produced by these two apertures and calculating the relative contributions of isotropic diffuse returns and narrow specular reflections (Section 2.5 and Chapter 3 treat this method in greater detail). The specularity is calculated along each survey line and 5 km gridded specularity maps are produced for each of the two survey directions in addition to a specularity map from the average of these two orthogonal orientations, which is a proxy for the portion of the bed covered by specular reflectors with any orientation. I determined the major hydrologic pathways using gridded 5 km bed topography and ice surface elevation using steepest-descent to determine path direction [117]. For the pathway profiles, I extracted specularity content from the 5 km gridded total specularity data and determined relative echo strength by empirically performing a distance and loss correction to account for englacial attenuation across the catchment [34]. For the width-averaged plots, I extracted the surface profile from gridded surface elevations [9] and the basal shear stress from model-derived values [46] and averaged across the width of the glacier catchment. For the upstream subglacial melt-water plot, I used model-derived melt-water values [46], totaled

the upstream melt-water, and averaged across the width of the glacier catchment. I determined the location of the distributed to concentrated transition by investigating profiles across the entire catchment and identifying the point downstream of which the specularity and relative echo strength profiles stop tracking and begin to diverge with decreasing specularity.

2.5 Supporting information

2.5.1 Specularity content of radar returns

I use the angular distribution of energy in radar returns to identify and characterize water systems beneath Thwaites Glacier, West Antarctica. I exploit the radar scattering character of the planar interfaces of distributed subglacial water systems to identify them from the narrow angular distribution of their returned radar energy and to distinguish them from concentrated subglacial water systems with cylindrical interfaces that scatter energy over a wide range of angles. The metric I use to describe the angular distribution of echo energy on a continuum between specular reflection and diffuse scattering is the specularity content. In this work, I define the specularity content, S_c, in terms of two quantities the specular energy, S, which is the radar energy returned in a narrow angular distribution around the specular direction and the diffuse energy, D , which is the total energy isotropically scattered over the 180° half-space [71]. The *specularity content* is then the fraction of the total energy that is contributed by the specular component

$$S_c = \frac{S}{S + D} \tag{2.1}$$

so that a purely specular (or mirror-like) surface will have a specularity content of one and a purely diffuse surface (i.e. a point-scatter) will have a specularity content of zero.

2.5.2 Focusing with different apertures

In this work, I calculate the specularity content of radar returns by performing range-migrated synthetic aperture radar focusing on airborne ice penetrating radar data using two different focusing correlation aperture lengths, L_1 and L_2 (after [83]) (Figure 3.2). By focusing with two different apertures, I produce bed echoes that include radar energy that has been focused across two different spans of scattering angles, Φ_1 and Φ_2 (Figure 3.1). These angles can be determined from Snells law by solving

$$\frac{L/2 - x}{\sqrt{h^2 + (L/2 - x)^2}} = \frac{x\sqrt{\epsilon_r}}{\sqrt{d^2 + x^2}} \tag{2.2}$$

for the refraction point at the surface, x , where h is the survey height, d is the ice thickness, and ϵ_r is the relative permittivity of ice (after [38]). The range of scattering angles spanned by the focusing aperture is then given by

$$\Phi = 2\tan^{-1}(x/d) \tag{2.3}$$

The focused radar echo strengths for each aperture will include the energy scattered within the angle $\pm\Phi/2$ of nadir. By comparing these amplitudes for different focusing apertures, I constrain the angular distribution of echo energy and calculate the specularity content of the radar return from the bed. The specularity content is only a function of the angular distribution of echo

energy and is therefore independent of attenuation ambiguities from uncertain ice temperature and chemistry [63, 64].

2.5.3 Calculating specularity content

I calculate the specularity content of bed echoes for Thwaites Glacier, West Antarctica by focusing airborne ice penetrating radar data with two different focusing apertures, $L_1 = 700$ m and $L_2 = 2$ km. In calculating the specularity content, I assume that the entirety of the energy from the specular component is contained within the range of angles spanned by aperture L_1, which is a conservative assumption for the bed slopes (0 - 6°) and ice thicknesses (1 - 4 km) [41] that typify my study area. The echo strength, E_1, of radar returns focused using aperture L_1 will therefore include all of the energy in the specular component and a portion of the energy in the diffuse component (corresponding to the fraction of the half-space spanned by Φ_1) and given by

$$E_1 = S + D\frac{\Phi_1}{180^\circ} \tag{2.4}$$

Likewise the echo strength, E_2, of radar returns focused using aperture L_2 will include all of the energy in the specular component and a larger portion of the energy in the diffuse component (corresponding to the fraction of the half-space spanned by Φ_2) and given by

$$E_2 = S + D\frac{\Phi_2}{180^\circ} \tag{2.5}$$

The difference between these two echo strengths, ΔE, is the fraction of diffuse energy that was scattered at an angle greater than $\Phi_1/2$ but smaller than

$\Phi_2/2$. The total energy in the diffuse component, D, can be calculated from

$$\Delta E = E_2 - E_1 = D\frac{\Phi_2 - \Phi_1}{180^\circ} \tag{2.6}$$

as

$$D = \frac{180^\circ}{\Phi_2 - \Phi_1}(E_2 - E_1) \tag{2.7}$$

and the specular component, S, can be calculated using the echo strengths from either focusing aperture by combining Equation 2.7 with Equation 2.4 or Equation 2.5, giving

$$S = E_2 - D\frac{\Phi_2}{180^\circ} = E_1 - D\frac{\Phi_1}{180^\circ} \tag{2.8}$$

2.5.4 Interpreting specularity from a gridded survey

In this work, I calculate the specularity content for bed echoes along the survey lines for the gridded AGASEA airborne ice penetrating radar survey [41]. I produce 5- x 5- km gridded data products for each of the orthogonal survey directions. By comparing the specularity content for these two orthogonal directions, I am able to infer the anisotropy of the specularly reflecting interfaces at the bed (and infer that the distributed water systems at the bed are anisotropic). I also average gridded specularity values from the two orthogonal directions, which provides a rough constraint on the spatial distribution of specular interfaces across the catchment. This average specularity is a function of both the portion of the grid cell that is covered by specular reflecting interfaces (or distributed water) and the orientation of the survey grid with respect to any anisotropy in these interfaces. In other words, a change in

the specularity along either axis will result from a change in the along-track length of a reflecting interface [50] for any change in grid orientation. However, since the survey grid is orthogonal, the along-track reflector length and the specularity along the two axes of the grid will change complementarily (with one growing as the other shrinks) so the resulting average specularity will be much less sensitive to orientation than to the existence and areal extent of distributed water.

Chapter 3

Subglacial water geometry

Airborne radar sounding is an established tool for observing the bed conditions and subglacial hydrology of ice sheets and glaciers. The specularity content of radar bed echoes has also been used to detect the hydrologic transition of a subglacial water system from a network of distributed canals to a network of concentrated channels beneath Thwaites Glacier. However the physical dimensions of the distributed water bodies in these networks have not been constrained by observations. In this chapter, I use a variety of simple radar scattering, attenuation, and cross section models to provide a first estimate of the subglacial water body geometries capable of producing the observed anisotropic specularity of the Thwaites Glacier catchment. This approach leads to estimates of ice/water interface rms roughnesses less than about 15 cm, thicknesses of more than about 5 cm, lengths of more than about 15 m, and widths between about 0.5 and 5 m.

A version of this chapter is in review with *IEEE Geoscience and Remote Sensing Letters* under the title "Estimating subglacial water geometry using radar bed echo specularity: application to Thwaites Glacier, West Antarctica" with co-authors D. D. Blankenship, R. K. Raney, and C. Grima.

3.1 Introduction

Sounding ice sheets with airborne ice penetrating radar is a powerful and well established tool for probing the interior structures and bed configurations of glaciers and ice sheets [107, 28, 29, 37, 77, 27]. Glaciological and geophysical interpretations of ice penetrating radar records have advanced the observation and understanding of subglacial lakes and hydrologic systems [16, 79, 78, 83, 97]. These water systems can exert critical control on the behavior, evolution, and stability of marine ice sheets and their sea level contribution [96, 24, 112].

Traditional interpretation methods [79, 102, 34, 25, 17], which rely on identifying subglacial water bodies as flat and bright interfaces in radargrams, are susceptible to erroneous interpretation due to uncertainty in englacial attenuation from observationally underconstrained ice temperature and chemistry [63, 64, 65]. To address this challenge, the specularity content of radar bed echoes (a parameterization of the along-track scattering function expressed in its Doppler distribution [90, 89]) has been used to provide an attenuation-independent proxy for distributed subglacial water bodies [97]. These water bodies are in hydrostatic equilibrium with the overlying ice and their melt-freeze processes produce ice/water interfaces that are flat at the wavelength scale [78], resulting in specular radar reflections [97].

The anisotropic specularity of radar bed echoes has been used to detect a subglacial water system beneath the upstream region of Thwaites Glacier composed of a network of distributed canals [112] eroded into the subglacial

sediment [97]. Although their detection represents an unprecedented observation of the dynamically critical hydrologic state [24, 32, 112, 96] of subglacial water beneath a contemporary ice sheet, the geometry of the water bodies that make up these distributed networks have not been constrained by geophysical observation or analysis. The only know method for obtaining such observations is ice penetrating radar, yet the only prior use of radar sounding data to directly constrain the geometry of subglacial water bodies have been applied in East Antarctica [25] and Greenland [78]. These settings have fundamentally different topographic, lithologic, and geothermal basal boundary conditions from Thwaites Glacier in particular and West Antarctica in general and, as such, support different regimes and configurations of subglacial water [41, 46, 59, 11, 14, 112] .

It is the aim of this chapter to provide the first estimates of the unique physical properties that can be inferred in glaciological or geophysical interpretation of subglacial water systems that produce anisotropic specular bed echoes in airborne radar sounding data. Such estimates provide new and essential insights and are useful for understanding and modeling the behavior of subglacial water systems, their control on ice sheet evolution, and their comparison to the geologic, morphologic, and sedimentary record of the subglacial water systems of paleo ice sheets.

3.2 Specularity content of bed echoes

SAR focusing [87, 57, 55, 83, 38, 80, 118] of coherent radar sounding [13, 98, 68, 35, 69, 84] data is achieved by convolving the recorded data with a reference function for the phase history of a point scatterer at the bed. The propagation path between an airborne radar and a point on the ice-bed interface is shown in Figure 3.1 and described by

$$\frac{\frac{L}{2} - x}{\sqrt{h^2 + \left(\frac{L}{2} - x\right)^2}} = \frac{x\sqrt{\epsilon_r}}{\sqrt{d^2 + x^2}} \tag{3.1}$$

where L is the focusing reference aperture, h is survey height above the ice surface, d is the ice thickness, x is the displacement of the refraction point on the ice surface, and $\sqrt{\epsilon_r}$ is the index of refraction of ice [83, 38]. The

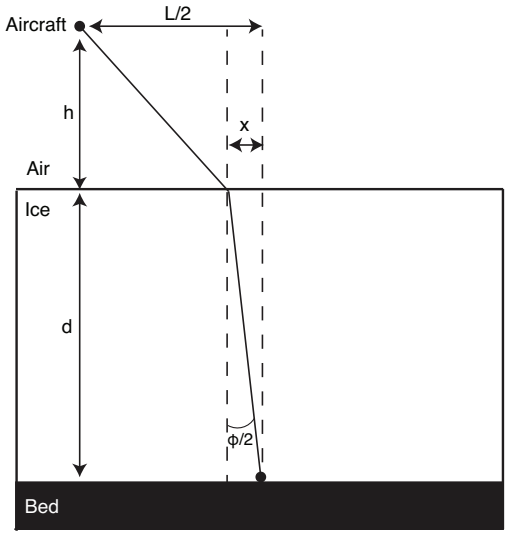

Figure 3.1: Geometry for the path of a radar return from a point on the ice/bed interface.

specularity content of a bed echo [97] is a parameterization that models the along-track scattering function as an angularly narrow specular component S (assumed to be narrower than the smallest focusing aperture used) (Figure 3.2a) and an isotropic diffuse component D (assumed to be uniform across the half-space at the bed) (Figure 3.2b) with the specularity content S_c of the bed echo given by

$$S_c = \frac{S}{S + D} \tag{3.2}$$

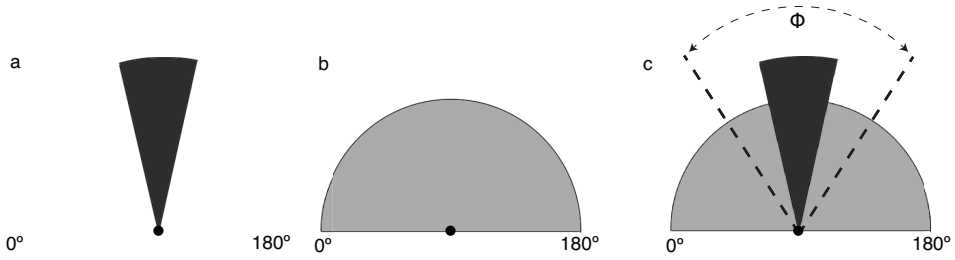

Figure 3.2: Model for the scattering function of (a) a purely specular reflecting interface, (b) a purely diffuse isotropically scattering interface, and (c) an interface that returns both diffuse and specular energy.

This value is calculated by focusing with two different focusing apertures L_1 and L_2 [83]. In this case, the angles spanned by each are Φ_1 and Φ_2 (Figure 3.2c) given by

$$\Phi = 2\tan^{-1}(x/d). \tag{3.3}$$

The energies focused by each are E_1 and E_2 and are given by

$$E_1 = S + D\frac{\Phi_1}{180^\circ} \tag{3.4}$$

and

$$E_2 = S + D\frac{\Phi_2}{180^\circ}, \tag{3.5}$$

so that the specularity content is

$$S_c = \frac{\frac{E_2}{E_2-E_1} - \frac{\Phi_2}{\Phi_2-\Phi_1}}{\frac{E_2}{E_2-E_1} + \frac{180-\Phi_2}{\Phi_2-\Phi_1}}. \tag{3.6}$$

Because both energies are focused through the same ice column, any loss from englacial attenuation will apply equally to both focused energies so that

$$E_1 = \left(S + D\frac{\Phi_1}{180^\circ}\right) 10^{ld/10} \tag{3.7}$$

and

$$E_2 = \left(S + D\frac{\Phi_2}{180^\circ}\right) 10^{ld/10}, \tag{3.8}$$

where l (in dB/km) is the englacial attenuation rate. Equations 3.6, 3.7, and 3.8 show that the calculated specularity is unchanged by the value of l. It follows that the specularity content of radar bed echoes is a measure of the angular spread of the along-track scattering function that is *independent of attenuation through the ice column.*

3.3 Roughness of ice/water interfaces

The specularity of a radar bed echo is determined, in part, by the roughness of the ice/water interface [62] (Figure 3.3). Under Kirchoff assumptions, the unfocused echo energy returned at nadir E_0 is a function of the rms height of the reflecting interface (here assumed to be water) RMS_w and is given by

$$E_0 = e^{-g^2} I_0^2 \left(g^2/2\right), \tag{3.9}$$

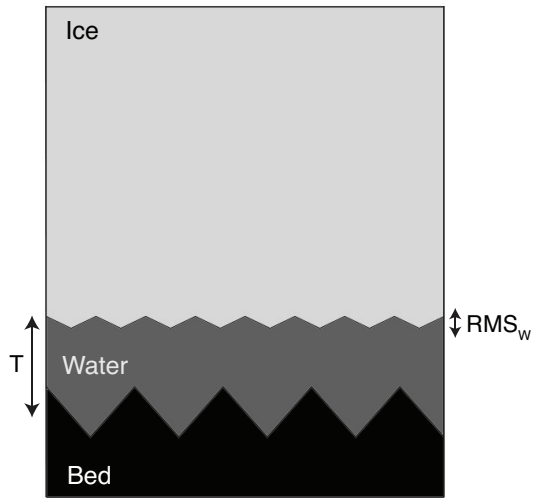

Figure 3.3: Cartoon of the roughness of the ice/water interface RMS_w of a subglacial water layer of finite thickness T.

where

$$g = 4\pi \,\mathrm{RMS}_w \, f_c \sqrt{\epsilon_r}/c, \tag{3.10}$$

and f_c is the central frequency of the radar, c is the speed of light in a vacuum, and I_0 is the modified zeroth order Bessel function of the first kind [84]. Alternatively, the scattering function of surfaces that satisfy Kirchoff assumptions can be modeled as a normal distribution of energy across scattering angles [71]. Since the energy is distributed normally, the unfocused echo energy returned at nadir can be calculated using an error function (erf) [62], given by

$$E_0 = \mathrm{erf}\left(\frac{1}{2g}\right)_a \mathrm{erf}\left(\frac{1}{2g}\right)_x \tag{3.11}$$

where erf_a models scattering in the along-track direction and erf_x models scattering in the across-track direction. Empirically, Equation 3.11 provides an ap-

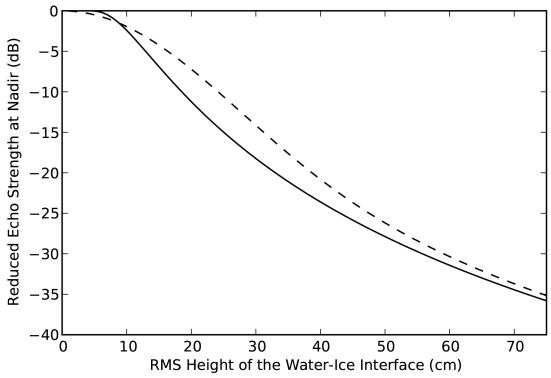

Figure 3.4: Reduction in reflected power at nadir as a function of surface roughness described by Equation 3.9 (dashed-line) and Equation 3.11 (solid line).

proximation for Eqution 3.9 (Figure 3.4). Notably, this approximation allows along-track focusing with different apertures to be easily modeled by changing the argument in the first error function (corresponding to scattering in the along-track direction).

$$E_i = \mathrm{erf}\left(\frac{\Phi_i/\phi_F}{2g}\right)\mathrm{erf}\left(\frac{1}{2g}\right), \tag{3.12}$$

where Φ_i (Equation 3.3) is the range of scattering angles spanned by the focusing reference aperture and ϕ_F (Equation 3.13) is the range of scattering angles spanned by the diameter of the 1^{st} Fresnel zone D_1 at the bed (corresponding to the range of scattering angles in the unfocused nadir return), given by

$$\phi_F = 2\tan^{-1}(D_1/2d) \tag{3.13}$$

and

$$D_1 \approx \sqrt{2c/f_c \left(h + \frac{d}{\sqrt{\epsilon_r}} \right)}. \tag{3.14}$$

With this model, the focused energies for each aperture are given by

$$E_1 = \text{erf}\left(\frac{\Phi_1/\phi_F}{2g} \right) \text{erf}\left(\frac{1}{2g} \right) \tag{3.15}$$

and

$$E_2 = \text{erf}\left(\frac{\Phi_2/\phi_F}{2g} \right) \text{erf}\left(\frac{1}{2g} \right) \tag{3.16}$$

and the specularity content is given by Equation 3.6. Figure 3.5 shows that, for a survey height of $h = 750$ m, an ice thickness of $d = 2$ km, and focusing apertures of $L_1 = 700$ m (the widest practical aperture without range migration) and $L_2 = 2$ km (the widest practical aperture without reaching the critical angle) (typical values for the Thwaites Glacier survey [97, 41]) high specularity values indicate an ice/water interface with rms heights less than about 15 cm.

3.4 Thickness of subglacial water layers

In order to estimate the minimum thickness T of a specularly reflecting water layer, I model the scattering function of the ice/water interface as purely specular and the scattering function of the water/bed interface as purely diffuse (the most pathological case for producing specular returns). I assume that the reflection coefficient for the ice/water R_w and water/bed R_b interfaces are determined by the real permittivity of the ice ϵ_i, water ϵ_w, and bed ϵ_b [84] and

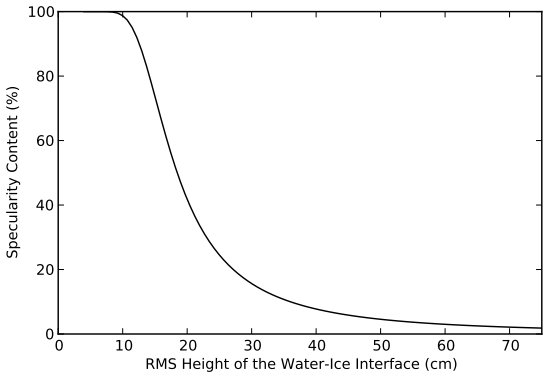

Figure 3.5: Specularity of radar bed echoes as a function of the roughness of the ice/water interface.

given by

$$R_w = \left| \frac{\sqrt{\epsilon_w} - \sqrt{\epsilon_i}}{\sqrt{\epsilon_w} + \sqrt{\epsilon_i}} \right| \tag{3.17}$$

and

$$R_b = \left| \frac{\sqrt{\epsilon_b} - \sqrt{\epsilon_w}}{\sqrt{\epsilon_b} + \sqrt{\epsilon_w}} \right| \tag{3.18}$$

We also assume that the specular component of the total bed echo is proportional to the reflection coefficient for the ice/water interface and increases exponentially with the fraction of the skin-depth (δ) occupied by the water layer thickness (T) (such that S = 0 for T = 0, S asymptotically approaches R_w as T approaches ∞, and S is decreased by e^{-1} at $T = \delta$ [25]), given by

$$S = R_w(1 - e^{-T/\delta}), \tag{3.19}$$

and

$$\delta = \sqrt{\frac{1}{\pi f_c \sigma_w \mu_0}}, \tag{3.20}$$

where σ_w is the conductivity of the water and μ_0 is the permeability of free space. I assume that the diffuse bed return is attenuated by the two-way path through the water layer and is given by

$$D = R_b e^{-2T/\delta} \tag{3.21}$$

and the specularity content of the total bed echo is given by Equation 3.2. Figure 3.6 shows that the depth of water required to produce specular returns is highly dependent on the conductivity σ_w of the subglacial water (and therefore its salinity and local geochemistry). Figure 3.6 also shows that (for $\epsilon_i = 3.17$, $\epsilon_w = 80$, $\epsilon_b = 18$, and $\sigma_w = 1$, which is typical of ground water [25, 94, 84]) specular water layers are expected to have thicknesses greater than about 5 cm.

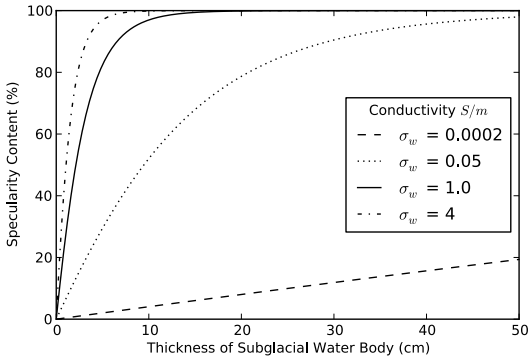

Figure 3.6: Specularity content of radar bed echoes as a function of water layer thickness T and conductivity σ_w (a σ_w value of about 0.0002 is typical of pure water, of about 4 is typical of sea water, and about 1 is typical of ground water [84, 25, 94]).

3.5 Length of subglacial water bodies

Because the water system in the upstream portion of the Thwaites catchment is a network of distributed canals, I can approximate the reflecting geometry of its ice/water interface as a rectangular plate (Figure 3.7) with radar cross section RCS [50] given by

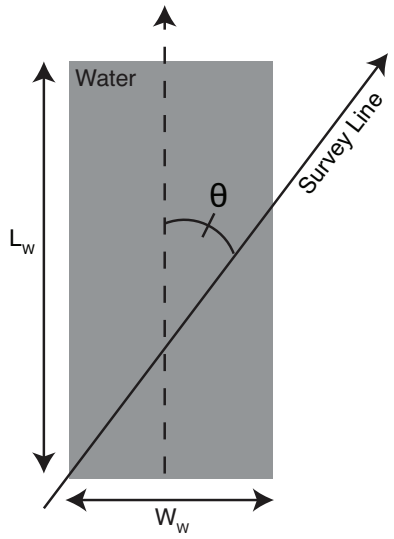

Figure 3.7: Observation geometry for a subglacial water body with a rectangular reflecting interface.

$$RCS \propto \frac{\sin^2(kL_w \sin\phi)}{k^2 L_w^2 \sin^2\phi} \tag{3.22}$$

for

$$\Theta = 0 \tag{3.23}$$

where Θ is the observation angle (the angle between the direction of water flow and the survey line), ϕ is the along-track scattering angle, L_w is the length of

the subglacial water body, and k is the wavenumber, given by

$$k = 2\pi f_c / c \tag{3.24}$$

In order to estimate the effect of water body length on bed echo specularity, I calculate the focused echo energies E_1 and E_2 by integrating the radar cross section across the range of scattering angles $\pm\Phi_1/2$ and $\pm\Phi_2/2$ spanned by the focusing apertures and given by

$$E_1 = \int_{-\Phi_1/2}^{\Phi_1/2} \frac{\sin^2(kL_w \sin\phi)}{k^2 L_w^2 \sin^2\phi} \delta\phi \tag{3.25}$$

$$E_2 = \int_{-\Phi_2/2}^{\Phi_2/2} \frac{\sin^2(kL_w \sin\phi)}{k^2 L_w^2 \sin^2\phi} \delta\phi \tag{3.26}$$

Figure 3.8 shows that specular subglacial water bodies are detectable (specularity content exceeds 0.5) for lengths greater than about 15 meters.

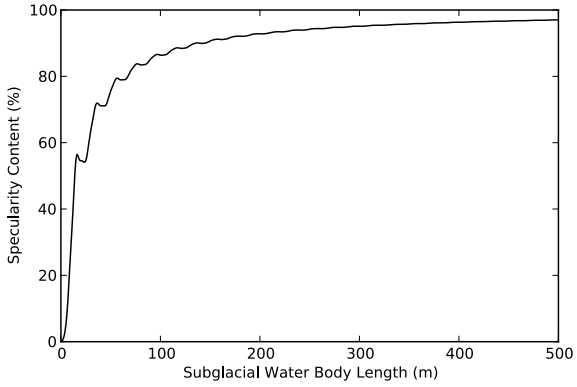

Figure 3.8: Specularity content of radar bed echoes as a function of subglacial water body length.

3.6 Width of subglacial water bodies

The distributed subglacial water systems observed beneath the upstream region of the Thwaites Glacier catchment are anisotropic [97] and produce bed echoes with specularity that varies as a function of observation angle. The rectangular plate model (Figure 3.7) for the radar cross section of a subglacial water body also varies as a function observation angle Θ and width W_w so that effective along-track length L_Θ is given by

$$L_\Theta = \begin{cases} \left|\frac{W_w}{\sin\Theta}\right| & \text{for } \Theta > \tan^{-1}(W_w/L_w) \\ \left|\frac{L_w}{\cos\Theta}\right|, & \text{for } \Theta \leq \tan^{-1}(W_w/L_w) \end{cases} \tag{3.27}$$

and the focused echo energies are given by

$$E_1 = \int_{-\Phi_1/2}^{\Phi_1/2} \frac{\sin^2(kL_\Theta \sin\phi)}{k^2 L_w^2 \sin^2\phi} \delta\phi, \tag{3.28}$$

and

$$E_2 = \int_{-\Phi_2/2}^{\Phi_2/2} \frac{\sin^2(kL_\Theta \sin\phi)}{k^2 L_w^2 \sin^2\phi} \delta\phi \tag{3.29}$$

and the specularity content is given by Equation 3.6. Figure 3.9 shows that (for a length $L_w = 300$ m) subglacial water bodies that appear specular within about 30° of ice flow and diffuse in the other can be estimated to have widths between about 50 cm and about 5 m.

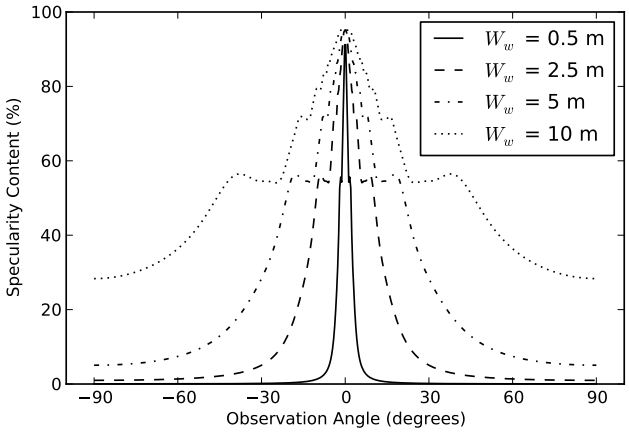

Figure 3.9: Specularity content of radar bed echoes as a function of observation angel Θ_w and water body width W_w.

3.7 Conclusions

Although the scattering function and specularity of bed echoes of subglacial water result from a combination of these effects, these results provide the first estimate of the physical dimensions of subglacial water bodies that can be inferred from the anisotropic specularity of bed echoes. I estimate that the subglacial water bodies in the upstream region of Thwaites Glacier, West Antarctica have ice/water interfaces with rms roughnesses less than about 15 cm, depths of more than about 5 cm, lengths from about 15 m to more than 75 m, and widths of between about 50 cm and 5 m.

Chapter 4

Deformable sediments and exposed bedrock

The geologic and morphologic records of prior ice sheet configurations show evidence of rapid, back-stepping, meltwater intensive retreats. The potential for such a retreat in a contemporary glacier depends on the rheology and lithology of the current ice sheet bed, which lies beneath kilometers of ice, making its physical properties difficult to charaterize. I use radar sounding and marine bathymetry data to compare the bed configurations of Thwaites Glacier and the paleo Pine Island Glacier. Using bed morphology and radar scattering, I show that the tributaries and upper trunk of Thwaites Glacier are underlain by ice-flow aligned bedforms of deformable sediment and that the lower trunk is grounded on a region of exposed bedrock. This is the same configuration as the paleo Pine Island Glacier during its relatively rapid, meltwater intensive retreat across the inner continental shelf, suggesting that Thwaites Glacier may be poised to experience a retreat with similar character and pacing.

A version of this chapter is in review with *Geophysical Research Letters* under the title "Airborne radar sounding reveals pervasive deformable sediments with significant bedrock buttressing beneath Thwaites Glacier, West Antarctica" with co-authors D. D. Blankenship, D. A. Young, A. E. Witus, and J. B. Anderson.

4.1 Introduction

Thwaites Glacier lies in the ASE of the marine WAIS and is one of the largest, most rapidly changing glaciers on earth [19, 54, 93]. Its landward sloping bed reaches into the deep interior of the ice sheet [41], making it a leading component in deglaciation scenarios [9]. Improved predictions of the contribution of the WAIS to future sea level require assessing the potential that Thwaites Glacier will experience an unstable retreat [104]. Recent acceleration in the ASE in general and the Thwaites Glacier catchment in particular have been correlated with warm ocean water, thought to accelerate ice flow and mass loss by reducing buttressing and eroding ice near the grounding zone [86, 92]. The magnitude and sensitivity of the response to this forcing, however, depends on the lithologic and rheologic configuration of the ice sheet bed [82, 1].

Shipborne acoustic bathymetric mapping of paleo ice streams on deglaciated continental shelves have been analyzed to infer the configurations and processes associated with past ice sheet retreats [75, 26, 43, 52, 61, 73, 115]. Thwaites Glacier and Pine Island Glacier once converged on the outer continental shelf of the ASE, sharing a single gronding line as part of the paleo Pine Island Glacier [Figure 4.1a]. Morphologic and geologic records [39, 49, 60, 43, 73, 116] show that paleo Pine Island Glacier initially retreated across a region of deformable sediments, leaving ice-flow aligned lineated bedforms [Figure 4.1c]. After crossing a sedimentary to crystalline bedrock transition on the inner continental shelf [solid white line Figure 4.1a] it progressed in a relatively rapid, back-stepping, meltwater intensive, retreat across exposed

bedrock [Figure 4.1b] with a network of interconnected channels (occupied by concentrated subglacial meltwater for some or all of its retreat across $\sim$ 350 km of bedrock) [116, 45]. Today, Pine Island Glacier is grounded inland of that bedrock region on a landward sloping bed [31] with actively eroding sediments [70, 44, 103].

Recent observations show that Thwaites Glacier has also been stepping back across a series of bedrock ridges and is currently grounded on one of them [108]. The initiation and ultimate extent of a retreat from this position will be controlled by the details of ocean forcing [6], grounding zone hydrology [113], and shear margin stability [62]. However, the pacing and character of such a retreat will depend on the rheology and lithology of the bed upstream of the grounding line [82, 20]: specifically whether Thwaites Glacier will continue to retreat across exposed bedrock or will instead retreat across a bed of deformable sediments.

4.2 Methods

In order to investigate the basal lithology of Thwaites Glacier, I use radar sounding to characterize two regions of the bed: 1) the lower trunk (downstream of the dashed white line in Figure 4.1a) which has channelized subglacial water [97] and high basal shear stress [46] and 2) the upper trunk and tributaries (upstream of the dashed white line) which have distributed subglacial water and low basal shear stress. I present focused radar profiles [Figure 4.2b-f] from a gridded airborne radar sounding survey of the Thwaites

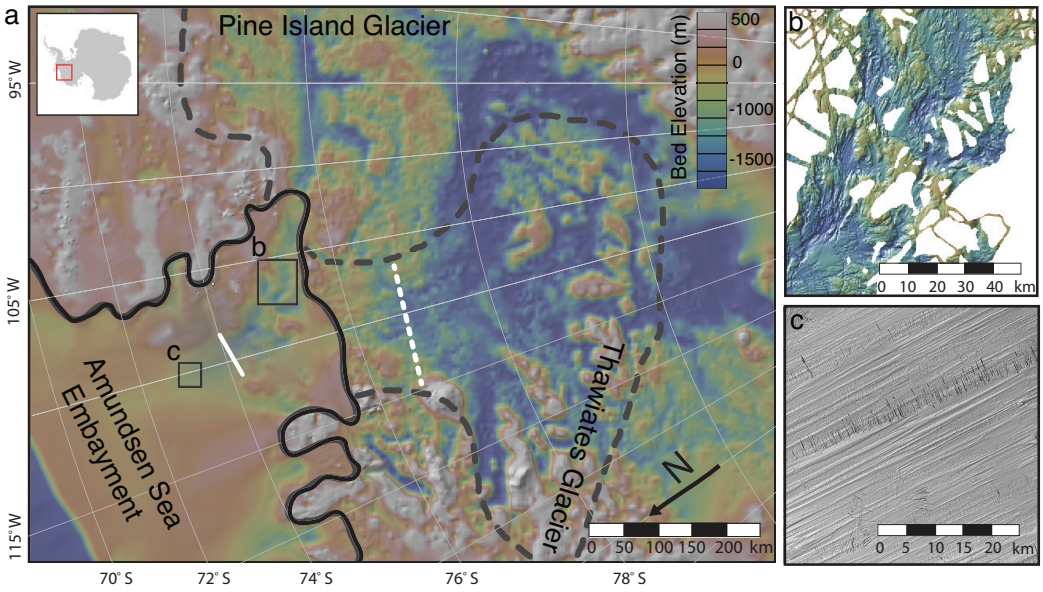

Figure 4.1: Bathymetry and bed topography [7] of the (a) ASE, including the sediment to bedrock transition on the inner continental shelf (solid white line) [49] and the distributed to concentrated subglacial water system transition beneath Thwaites Glacier (dashed white line) [97]. Bathymetry of the (b) exposed bedrock on the inner continental shelf [73] and (c) lineated sedimentary bedforms on the outer continental shelf [42, 5].

Glacier catchment [41] and compare the morphology, scale, and anisotropy of imaged bedforms with those of exposed bedrock [Figure 4.1b] and lineated sediments [Figure 4.1c] in shipborne acoustic bathymetry from the ASE continental shelf [42, 5, 73].

Since the radar generates profiles only along flight lines, which are separated by 15 km, I use the anisotropy of radar scattering from the gridded survey to infer the distribution of flow-aligned bedforms across the entire catchment. By calculating the bed-echo specularity [97] for orthogonal survey directions, I

determine the axis of symmetry for areas that are both anisotropic (where the difference in specularity between survey directions is greater than 40% of the mean) and have low average specularity content (below 17.5%, reflecting bedform rather than water body anisotropy). I plot the radar-derived direction of anisotropy in the context of ice surface speed [93] to show that the bedforms are aligned with ice-flow [Figure 4.3a].

Angularly dependent specularity is affected by bedform shape, size, and anisotropy. By plotting the specularity of bed echoes as a function of observation angle (the angle between survey and ice flow directions) I compare the relative anisotropy of the downstream and upstream (of the dashed white line in Figure 4.1a) regions of the Thwaites Glacier bed [Figure 4.3b and Figure 4.3c]. I also compare the angularly dependent specularity of the upstream region to the expected radar scattering from a sinusoidally corrugated bed [76] with heights, widths, and surface textures from radar sounding (Figure 2d-f and [48]), marine bathymetry [42, 58], and remote sensing [100] observations of lineations and sediments [Figure 4.3ci-iii].

Finally, I compare the specularity for the upstream and downstream regions of Thwaites Glacier to modeled angularly dependent specularity [Figure 4.3d and Figure 4.3e] using the observed bathymetries of exposed bedrock and lineated sediment [Figure 4.1b and Figure 4.1c respectively] on the deglaciated continental shelf of the ASE [43, 73, 5] using a simple geometric optics model [71] and assuming an ice thickness of 750 m and survey height of 500 m above the ice surface.

4.3 Radar inferred bedforms and lithology

Marine bathymetric observations of the deglaciated paleo Pine Island Glacier provide two distinct potential configurations for the contemporary bed of Thwaites Glacier. The first candidate configuration has a layer of deformable sediments which can stabilize grounding zones [82, 20] and form anisotropic ice-flow aligned lineated bedforms [42]. This bed configuration is characteristic of numerous paleo-ice streams [58] including paleo-Pine Island Glacier from the Last Glacial Maximum until ∼10.3 kya [49] (seaward of the solid white line in Figure 4.1a) as well as the contemporary bed of the Rutford Ice Stream [48]. The second candidate configuration is a bed of exposed bedrock with a network of interconnected meltwater channels across which retreat tends to occur relatively rapidly, back-stepping across bedrock highs [49, 108, 82]. This was the bed configuration for the paleo-Pine Island Glacier at ∼7 kya [49] (landward of the solid white line in Figure 4.1a).

The lower trunk region of Thwaites Glacier (downstream of the dashed white line in Figure 4.1a) has been observed to have high basal shear stress [46] and channelized subglacial water [97] suggesting that the bed in this region may be a continuation of the exposed bedrock on the inner continental shelf across which paleo Pine Island retreated. The along-flow [Figure 4.2b] and across-flow [Figure 4.2c] radar profiles in this region show rough bedforms in both directions with scales and mophology consistent with the deglaciated bedrock in the ASE [Figure 4.1b]. The angularly dependent specularity of this region [Figure 4.3b] also shows the area to be isotropically rough and consistent

with modeled angularly dependent specularity using the bathymetry data for that region [Figure 4.3d].

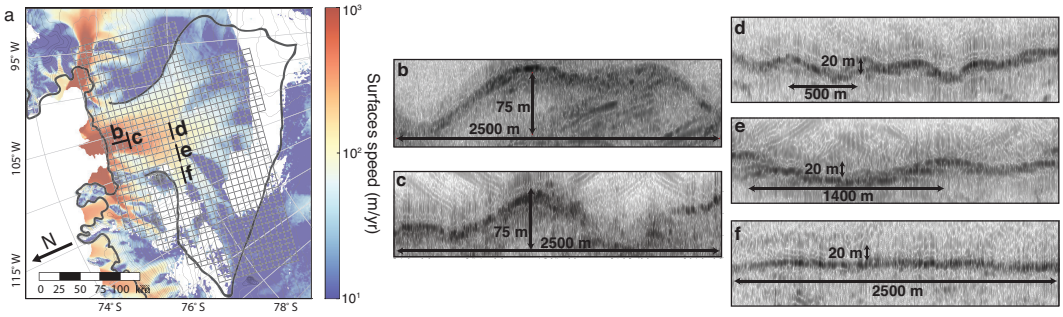

Figure 4.2: Radar profiles from a gridded airborne survey of (a) the Thwaites Glacier catchment, showing the along flow (b) and across flow (c) bedforms of the downstream region as well as the across-flow (d), oblique-to-flow (e), and along-flow (f) bedforms of the upstream region.

The tributaries and upper trunk of Thwaites Glacier (upstream of the dashed white line in Figure 4.1a) have been observed to have low basal shear stress [46] and distributed subglacial water [97] suggesting that the bed may have a layer of deformable sediments [112, 32]. Radar profiles collected perpendicular [Figure 4.2d], oblique [Figure 4.2e], and parallel [Figure 4.2f] to ice flow show corrugated bedforms with crest-to-trough heights of $\sim$ 20 m and crest-to-crest widths of $\sim$ 500 m, which are similar in scale to lineated sedimentary bedforms (i.e. mega-scale glacial lineations) observed elsewhere [58, 48, 42]. The angularly dependent specularity of the upstream region of Thwaites Glacier is also consistent with anisotropic [Figure 4.3c] ice-flow-aligned bedforms with higher specularity values for smaller observation angles. This pattern is consistent with the modeled specularity response from the bathymetry of lineated

sediments in the ASE continental shelf [Figure 4.3d]. Airborne radar sounding of the upstream region of Thwaites Glacier also exhibits a distribution of specularity consistent with radar scattering modeled for corrugated sinusoidal surfaces with heights, widths, and rms slopes typical of subglacial lineated sediments [Figure 4.3c].

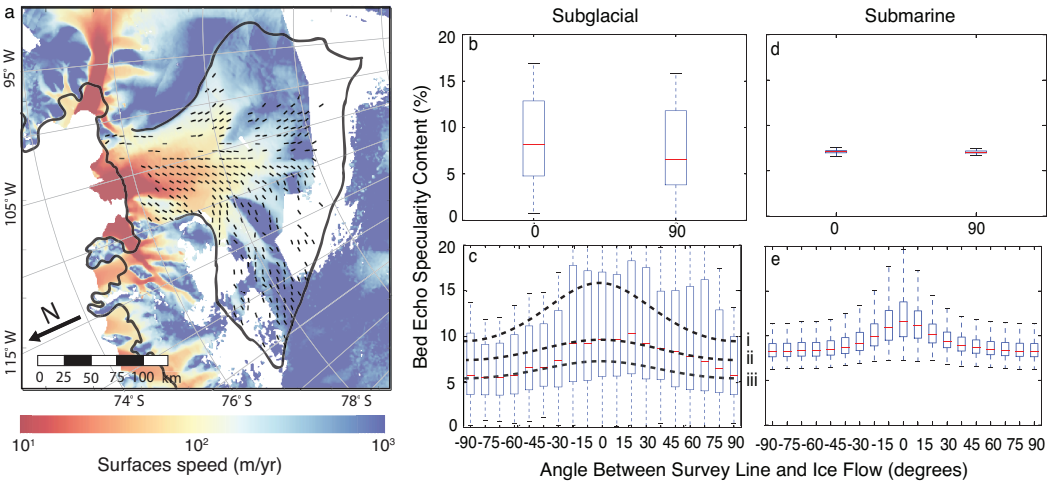

Figure 4.3: Anisotropy of bedform radar scattering. (a) Axis of symmetry (aligned with black dashes) for anisotropic, low specularity areas in the context of ice flow [93]. Angularly dependent specularity for the downstream (b) and upstream (c) regions of the Thwaites Glacier bed. Analytic specularity response for a sinusoidally corrugated sedimentary bed [100] with crest-to-trough heights, crest-to-crest widths, and surface texture rms-slopes of (i) 150 m, 6 m, and 7.5° (e.g. the ASE continental shelf (Figure 4.1c) [42]), (ii) 300 m, 10 m, and 9° (e.g. Rutford Ice Stream [48]), (iii) 500 m, 20 m, and 10° (e.g. upstream Thwaites Glacier (Figure 4.2d). Modeled specularity for bathymetry of (d) exposed bedrock (Figure 4.1b) and (e) lineated sediments (Figure 1c) on the ASE continental shelf.

4.4 Conclusions

We conclude that the tributaries and upper trunk of Thwaites Glacier are underlain by ice-flow aligned lineated bedforms of deformable sediment and that the lower trunk is grounded on a region of exposed bedrock lacking any significant sediment cover. Notably, this is the same configuration as paleo Pine Island Glacier during its relatively rapid, back-stepping, meltwater intensive, retreat across exposed bedrock on the inner continental shelf. This similarity raises the possibility that Thwaites Glacier may be poised to experience a retreat that is similar in character and pacing across its lower trunk region. It also suggests that, prior to its retreat, the paleo-Pine Island Glacier may have hosted a subglacial water system similar to the one observed beneath contemporary Thwaites Glacier.

4.5 Supporting information

4.5.1 Bedform orientation from anisotropic specularity

The specularity content of radar echoes measure the angular distribution of energy in the along-track direction and has been used to detect flat distributed water interfaces at the ice sheet bed [97]. By computing bed echo energies E_1 and E_2 using two different focusing correlation aperture lengths, L_1 and L_2 [83], which span scattering angles Φ_1 and Φ_2, I compute the distributed energy D in the bed echo as

$$D = \frac{180^\circ}{\Phi_2 - \Phi_1} \left(E_2 - E_1 \right), \tag{4.1}$$

the specular component of the bed echo as

$$S = E_2 - D\frac{\Phi_2}{180^\circ} = E_1 - D\frac{\Phi_1}{180^\circ}, \tag{4.2}$$

and the specularity content S_c as

$$S_c = \frac{S}{S+D}. \tag{4.3}$$

The geometry and roughness of the ice sheet bed also affect the angular distribution of scattered radar energy, which is expressed in the specularity content [76, 83, 97]. The orthogonal survey of Thwaites Glacier makes it possible to compare the specularity (and therefore bed roughness) in each direction. I determine the specularity for the entire survey [97] and produce gridded specularity maps for each survey direction (with 5- x 5- km grid cells). From these two gridded data sets, I select the cells that are anisotropic ($A > 0.4$) and have low average specularity ($S_{ave} < 0.175$), where

$$A = \frac{|S_{NS} - S_{EW}|}{(S_{NS} + S_{EW})/2}, \tag{4.4}$$

$$S_{ave} = (S_{NS} + S_{EW})/2, \tag{4.5}$$

and S_{NS} and S_{EW} are the specularity content values in the North-South and East-West survey grid directions. I determine the axis of symmetry for the selected cells by assuming that, for these regions, the average specularity is constant so that the angle of the axis of symmetry Θ_{spec} is given by

$$\Theta_{spec} = tan^{-1}(S_{EW}/S_{NS}), \tag{4.6}$$

which corresponds to the direction of bedform orientation.

The angle of the anisotropic specularity has four ambiguous values (as a result of the tan^{-1}) but since I am interested in the direction (rather than the angle) of anisotropy, there are only two ambiguous potential directions. I resolve this ambiguity by mirroring the direction across the center flow line of the glacier, which produces values that vary smoothly across the glacier and avoid physically unrealistic discontinuity and divergence at the center line. I plot the resulting direction in the context of ice flow [93].

4.5.2 Angularly dependent bed echo specularity

For anisotropic bed geometries, the along-track specularity content varies as a function of the observation angle Θ_{obs}, given by

$$\Theta_{obs} = \Theta_{line} - \Theta_{ice}, \tag{4.7}$$

where Θ_{line} is the direction of the airborne survey line and Θ_{ice} is the direction of ice flow from InSAR derived surface velocities [93]. I plot the specularity of each observation in the upstream region as a function observation angle. Because the upstream region includes a wider range of ice flow directions (and therefore samples a wider range of observation angles) I create a box plot for each 10° interval between $-90°$ and 90° in the upstream region and two box plots (parallel and perpendicular to ice flow) for the downstream region.

4.5.3 Angularly dependent specularity of a corrugated bed

To compare the physical scale of lineated bedforms with the angularly dependent specularity observed in the upstream region of Thwaites Glacier, I

use a simple two-scale scattering model [76] for a surface that is sinusoidally corrugated at large scales and has a rough surface texture at small scales. This surface is defined by a crest-to-trough height H, crest-to-crest width w, and a surface texture rms slope $\sigma_{texture}$. As the observation angle Θ_{obs} changes, along-track profiles of this surface can be modeled as sine waves with crest-to-trough heights H_Θ of

$$H_\Theta = H \tag{4.8}$$

and crest-to-crest widths w_Θ of

$$w_\Theta = \frac{w}{sin\left(\frac{\Theta_{obs}}{180°\pi}\right)}, \tag{4.9}$$

which correspond to bedform-scale rms slopes σ_{bed} [100, 76] of

$$\sigma_{bed} = tan^{-1}\left(\frac{\pi h sin\left(\frac{\Theta_{obs}}{180°\pi}\right)}{w\sqrt{2}}\right)\frac{180°}{\pi} \tag{4.10}$$

and a total combined (both bedform and surface texture) rms slope σ_{total} [76] of

$$\sigma_{total} = \sqrt{\sigma_{bed}^2 + \sigma_{texture}^2}. \tag{4.11}$$

We model the return from this surface as a gaussian scattering function [71] so that the echo energy E_i focused with an aperture that spans a range of scattering angles equal to Φ_i is

$$E_i = \text{erf}\left(\frac{\Phi_i}{\sigma_{total}}\right) \tag{4.12}$$

where erf is the error function [62] and the specularity content S_c (for focusing apertures that span the along-track scattering angles Φ_1 and Φ_2) is given by Equations 4.1 - 4.3.

4.5.4 Modeled specularity from bathymetry data

We use bathymetric observations [73, 42, 5] of the deglaciated continental shelf in the ASE to simulate the specularity content for these regions as if they were covered by ice and observed by airborne radar sounding. In these simulations, I use a simple geometric optics model [76] to predict the angular distribution of echo energy from facets in the gridded bathymetry. In this model, the energy E_i focused with an aperture that spans a range of scattering angles Φ_i is proportional to the fraction of facets within a pulse-limited footprint [84] that have along-track slopes within $\pm\Phi_i/2$ of nadir. For these simulations, I assume an ice thickness of 750 m and a survey height of 500 m. For the sedimentary region, I model observation angles from $-90°$ to $90°$, producing box plots at $10°$ intervals (to compare with the upstream region of Thwaites) and for the bedrock region I produce box plots for only perpendicular and parallel observation angles (to compare with the downstream region).

Chapter 5

Heterogenous geothermal flux

Heterogenous hydrologic, lithologic, and geologic basal boundary conditions can exert strong control on the evolution, stability, and sea level contribution of marine ice sheets [15, 106, 82, 110]. Geothermal flux is one of the most dynamically critical ice sheet boundary conditions, but is extremely difficult to constrain at the scale required to understand and predict the behavior of rapidly changing glaciers [66, 99]. This lack of observational constraint on geothermal flux is particularly problematic for the glacier catchments of the West Antarctic Ice Sheet (WAIS) within the low topography of the West Antarctic Rift System (WARS) where geothermal fluxes are expected to be high, heterogeneous, and possibly transient [10, 59, 12, 15]. Here, I use airborne radar sounding data [97] with a subglacial water routing model [53] to estimate the distribution of basal melting and geothermal flux beneath Thwaites Glacier, West Antarctica. I show that the Thwaites Glacier catchment has a minimum average geothermal flux of $\sim 114 \pm 10$ mW/m^2 with areas of high flux exceeding 200 mW/m^2 consistent with hypothesized rift-associated

A version of this chapter is in review with the *Proceedings of the National Academies of Science of the United States of America* under the title "Evidence for Elevated and spatially variable geothermal flux beneath the West Antarctic Ice Sheet" with co-authors D. D. Blankenship, D. A. Young, and E. Quartini.

magmatic migration [59] and volcanism [10]. These areas of highest geothermal flux include the western-most tributary of Thwaites Glacier adjacent to the subaerial Mount Takahe volcano [81, 56, 10] and the upper reaches of the central tributary near the WAIS Divide ice core drilling site [22].

5.1 Introduction

Heterogeneous geothermal flux and subglacial volcanism have the potential to modulate ice sheet behavior and stability by providing a large, variable supply of meltwater to the subglacial water system, lubricating and accelerating the overlying ice [110, 96]. However, the magnitude and spatial pattern of geothermal flux is extremely difficult to measure and the catchment-scale constraints derived from seismic tomography [99] and satellite magnetometry [66] produce contradicting spatial patterns and cannot resolve geothermal features relevant to local ice sheet forcing. Despite strong evidence for magma migration [59] and volcanism [10, 14, 59, 12] beneath the WAIS, the limitations of these heterogeneous estimates have lead modeling studies to assume unrealistic spatially uniform geothermal flux distributions [46, 51]. Accurate modeling of ice sheet contributions to sea level, site selection for ice core drilling, and enhanced understanding of ice-mantle interactions all require more accurate higher resolution estimates of the spatial distribution of geothermal flux across critical glacier catchments than are currently available.

Thwaites Glacier is one of the largest, most rapidly changing glaciers on earth and its landward sloping bed reaches into the deep interior of the WAIS,

making it a leading component in scenarios for rapid deglaciation [41, 46]. In addition, the catchment of Thwaites Glacier (Figure 1a) also lies within the WARS, a potentially reactivated Cretaceous intracontinental extension zone of low topography where rift-related thinning of the crust produces elevated geothermal flux [14, 10, 23, 59, 15]. Given the setting and configuration of its catchment, heterogenous geothermal flux beneath Thwaites Glacier is likely a significant factor in local, regional, and continental scale ice sheet stability. Thwaites Glacier has been observed by a catchment-wide airborne radar sounding survey [41]. To date, the use of radar sounding data to constrain melt rates has been limited to the interpretation of bed-echo strengths [84, 14] to indicate basal water or radar layer drawdown to estimate melted ice loss at the bed [30]. However, the interpretation of layer drawdown relies on the existence, persistence, and interpretability of layers in radar sounding profiles as well as constrained accumulation rates [30]. Further, the radar bed echo strength is affected by a combination of the material and geometric properties of the ice sheet and bed which introduce ambiguities in quantitative echo interpretation [63, 62, 64, 84]. Fortunately, the upstream portion of Thwaites Glacier is known to be underlain by a well quantified subglacial water system of distributed canals [97]. Distributed canals have relatively constant average depths [112] and their reflecting interfaces can be modeled as flat plates [97, 50]. Therefore, geometrically corrected [84] relative bed-echo strengths in the upstream region of Thwaites Glacier will be proportional to the areal coverage [50] and local flux of subglacial water. This specific knowledge of

the subglacial interface can be used to overcome the limitations of radar bed-echo interpretation and unambiguously establish meltwater quantities with well bounded uncertainties.

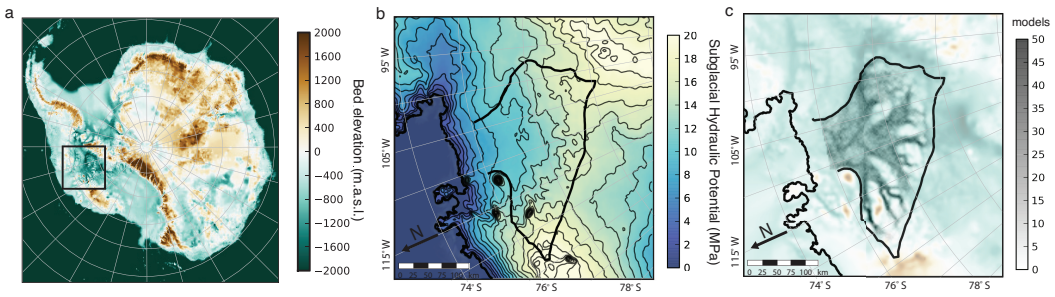

Figure 5.1: (a) Bed topography of the West Antarctic Ice Sheet and Amundsen Sea Embayment [33]. (b) Subglacial hydrologic potential [53] for a distributed water system in the upstream region of the Thwaites Glacier catchment (black boundary). (c) Collection of subglacial water routing models that best fit the observed radar bed-echo strength distribution (Figure 5.2a), where the darkness of grayscale cells is the number of models (out of 50) for which these cells drain at least 10 others upstream.

5.2 Results

In this analysis, I determine the mean and confidence interval uncertainties for englacial attenuation rates [34] (for both scattering and reflecting spreading geometries [84]) to produce maps of the mean (Figure 2a) and range (Figure 2b) of observed relative bed-echo strengths. Because distributed water is in pressure equilibrium with the overlying ice, its routing will be determined by the subglacial hydrologic potential, calculated using radar derived ice thickness and surface slope [53, 33] (Figure 1b). I generate a collection of water

routing models by adding noise (at the scale of gridding uncertainties) to the bed topography and selecting those routes that best fit the relative bed-echo strengths using uniform melt (Figure 3c). I use these routing models to determine the spatial distribution of melt required to reproduce the pattern of relative echo strengths (Figure 2a). I then scale the relative melt distribution by the spatial average and variance of routed subglacial water [53, 40] using the total melt from an ice sheet model of the Thwaites Glacier catchment [46]. This ice sheet model includes frictional heating, horizontal advection, and an assumed uniform geothermal flux [46]. Finally, I subtract the net effect of friction and advection to estimate the geothermal flux required to produce the remaining melt (Figure 5.3).

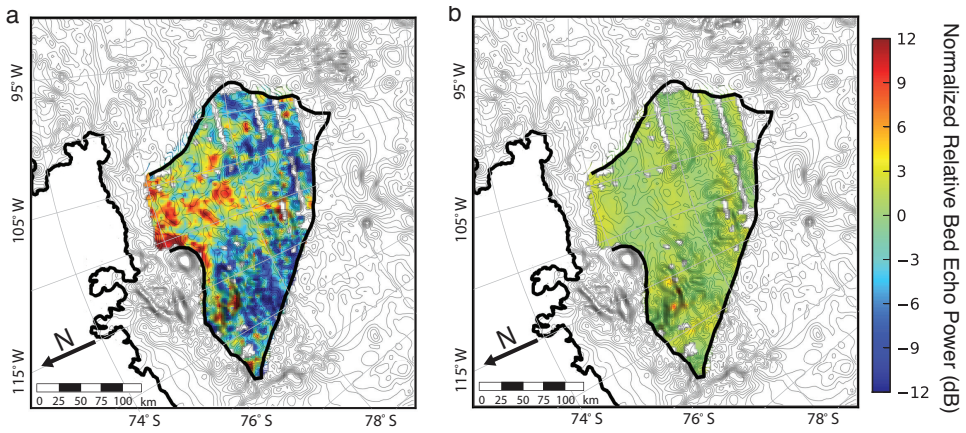

Figure 5.2: (a) Mean estimate of observed relative radar bed-echo strengths for the Thwaites Glacier catchment (black boundary) corrected for geometric spreading losses. (b) Range of estimates of corrected relative bed-echo strengths. Minor banding is due to variations in aircraft height above the ice surface combined with the different geometric loss terms. Bed topography [33] contour interval for Antarctica is 180 m.

The upstream region of the Thwaites catchment contains several areas of strong bed-echoes (Figure 5.2a) that exceed the mean bed-echo strength by significantly more than the uncertainty in those strengths (Figure 5.2b). Because the water system in this portion of the catchment is composed of distributed canals [97], high echo strengths can be interpreted as indicating larger quantities of subglacial water. The basal melt distribution required to fit the observed bed-echo strengths shows that water routing explains some of the strong reflections (and inferred high water quantities) in the trunk. The distribution of melt and geothermal flux (Figure 5.3) includes several regions with high melt that are closely related to known rift structure and associated volcanism [10, 12]. These include the western-most tributary (Figure 5.3c) that flanks Mount Takahe (Figure 5.3a), a subaerial volcano active in the Quaternary [81, 56], and several high flux areas across the catchment adjacent to topographic features that are hypothesized to be volcanic in origin [10, 12] (e.g. 5.3d and Figure 5.3e). High geothermal flux are also observed in the upper reaches of the central tributaries relatively near the site of the WAIS Divide ice core (Figure 5.3b), where unexpectedly geothermal flux has been inferred [22]. I estimate a minimum average geothermal flux value of $\sim$114 $\pm$ 10 mW/m^2 for the Thwaites catchment with areas exceeding 200 mW/m^2 (Figure5.3). These values are likely underestimates due to the low geothermal flux value used in the ice sheet model [46] and the effect of enhanced vertical advection of cold ice in high melt areas. Note that this latter effect also predicts a subtle gradient of underestimated flux from the interior to the trunk.

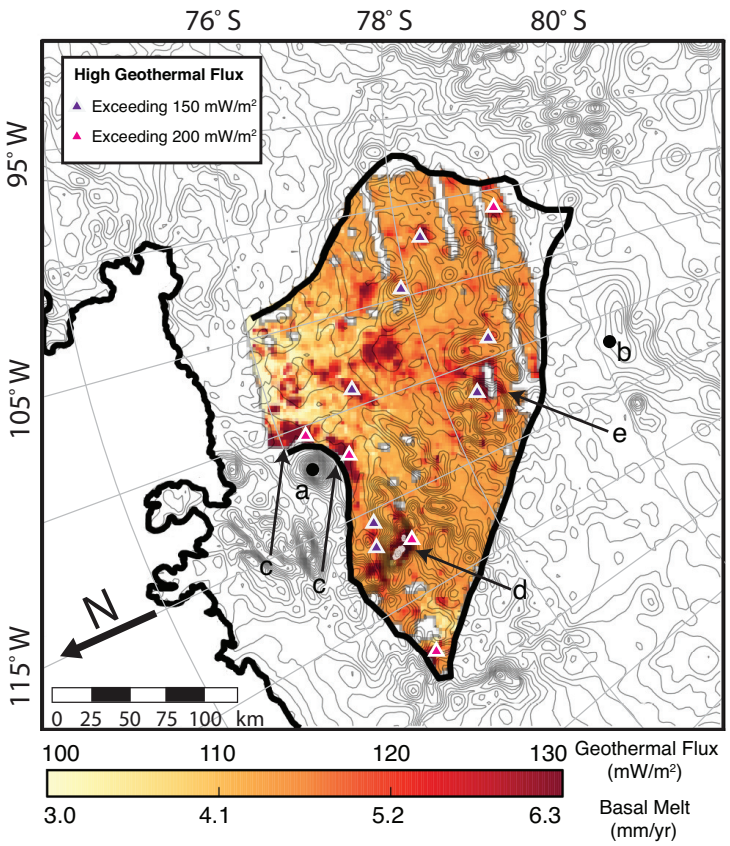

Figure 5.3: Minimum geothermal flux and basal melt values required to reproduce the observed relative bed-echo strengths (Figure 2a) with subglacial water routing models [53, 40] (Figure 1c) using the total melt water from an ice sheet model for the upstream portion of the Thwaites Glacier catchment [46]. The minumum average inferred flux is $\sim$114 $\pm$ 10 mW/m^2. High flux areas exceed 200 mW/m^2. (a) The Mount Takahe volcano. (b) WAIS Divide ice core drilling site. High melt areas (c) in the western-most tributary, (d) adjacent to the Crary mountains, and (e) in the upper portion of the central tributaries [10]. Triangles show areas where radar-inferred melt anomalies exceed those generated by ice dynamics (friction and advection) [46] and inferred geothermal flux exceeds 150 mW/m^2 (dark magenta) and 200 mW/m^2 (light magenta). Bed topography [33] contour interval for Antarctica is 180 m.

5.3 Conclusions

Above, I use radar echo strengths to constrain a subglacial water routing model to estimate the pattern of basal melting and geothermal flux for the Thwaites catchment. The simplifying assumptions in this analysis are rooted in specific knowledge of the geometry of the subglacial water system in this area [97] and conservative treatment of radar echo strength uncertainties. The results produce high melt values adjacent to known volcanoes, as well as structures that are morphologically suggestive of volcanic origin [10, 12]. I believe that both the magnitude and spatial pattern of estimated geothermal flux reflect the geologic and glaciological reality of the Thwaites bed. Contrary to previous modeling [46], my also results show regions of high geothermal flux that are in substantial agreement with levels from ice core drilling near the Thwaites ice divide [22]. This new approach provides both higher resolution and more geologically realistic boundary conditions for ice sheet modeling than previous estimates from remote sensing techniques [66, 99]. These results also demonstrate an approach that can be applied to a variety of radar sounders (since it requires only platform stability and not absolute echo strengths) in areas known to host distributed subglacial water systems. My results further suggest that the subglacial water system of Thwaites Glacier may be responding to heterogenous and temporally variable basal melting driven by the evolution of rift-associated volcanism and supports the hypothesis that both heterogenous geothermal flux [14] and local magmatic processes [59] could be critical factors the future behavior of the WAIS.

5.4 Methods

5.4.1 Subglacial water flux and bed echo strengths

Distributed subglacial canals beneath the upstream region of Thwaites Glacier [97] will have relatively constant average depths because of the relatively uniform till grain sizes and ice surface slopes in this part of the catchment [112]. In this case, the fraction of the bed covered by distributed canals will be proportional to the quantity of water flowing through that area. Therefore the relative strength of radar returns from the subsurface will be proportional to the fraction of the bed covered by subglacial water [50] and the quantity of water flowing through the area.

In this analysis, I use radar data collected with a central frequency of 60 MHz, a bandwidth of 15 MHz, a pulse-length of 1 μs, a 6.4 kHz pulse repetition frequency, and peak transmitted power of 8 kW [84]. I processed these data by performing a series of 320 coherent summations followed by 5 incoherent averages and gridding the resulting echo strengths in a 5- x 5- km grid. I use only the portion of the grid that includes the upstream part of the catchment, which is underlain by a water system of distributed subglacial canals [97]. There are two primary sources of uncertainty that need to be estimated, corrected, and accounted for to map relative bed-echo strengths with accompanying uncertainties. The first is geometric spreading losses due to the unknown combination of reflection and scattering produced by the geometry of the basal interface [84]. The second is unknown englacial attenuation due to uncertain ice temperature and chemistry [63, 64].

5.4.2 Geometric spreading losses and englacial attenuation

Our goal is to provide constraints on the distribution of melt and geothermal flux based only on relative bed-echo strength, bed topography, and ice surface data. I use a statistical analysis of the variation of echo strengths as a function of ice thickness to estimate the range of possible englacial attenuation rates [34]. Before englacial losses can be estimated, however, correction must be made for geometric spreading γ , which scales as one over the range squared for reflecting interfaces γ_r (coherent backscatter) and one over the range to the fourth power for scattering interfaces γ_s (non-coherent randomized backscatter) [84], given by

$$\gamma_r = \frac{1}{\left(h + d/\sqrt{\epsilon_r}\right)^2} \tag{5.1}$$

and

$$\gamma_s = \frac{1}{\left(h + d/\sqrt{\epsilon_r}\right)^4} \tag{5.2}$$

where h is the survey height, d is the ice thickness, and $\sqrt{\epsilon_r}$ is the index of refraction for ice [84]. To be conservative, I include corrections for both cases in my analysis and calculate the mean (l_μ) and 99% confidence interval ($l^-_{99\%}$,$l^+_{99\%}$) values for the 2-way englacial attenuation rates l (in dB/km) for each of the geometric spreading cases (γ_r and γ_s) [111]. Using these six values, I calculate P'_μ, which is the mean of the corrected relative echo strengths, given by

$$P'_\mu = \frac{1}{6}\sum_{i=1}^{6} Z'_{P_i} \tag{5.3}$$

and P'_{range}, which is the range between the maximum and minimum corrected relative echo strengths, given by

$$P'_{range} = Z'_{P_{max}} - Z'_{P_{min}}, \tag{5.4}$$

where

$$Z'_{P_i} = \frac{P'_i - \mu_{P'_i}}{\sigma_{P'_i}}, \tag{5.5}$$

$$P'_i = P\gamma_i 10^{l_i d/10}, \tag{5.6}$$

P is the raw echo power, γ_i is the geometric spreading loss, l_i is the englacial attenuation loss, $\mu_{P'_i}$ is the mean across the upstream portion of the catchment, $\sigma_{P'_i}$ is the standard deviation across the catchment, and the subscript i is the index for 1 of the 6 attenuation/geometric scenarios (the mean, upper, and lower confidence interval values for both scattering and reflection geometric spreading loss cases). These values range from 7.26 to 7.31 dB/km for reflection spreading losses and 4.69 to 4.75 dB/km for scattering spreading losses.

5.4.3 Subglacial water routing

To interpret these relative echo strengths in the context of basal water quantities and melt rates, I compare them with the water quantities predicted by a subglacial water routing model assuming a distributed water system in hydrostatic equilibrium with the overlying ice [53]. In this case, the subglacial hydrologic potential Φ_h is given by

$$\Phi_h = \rho_i g s + (\rho_w - \rho_i) g d, \tag{5.7}$$

where ρ_w is the density of water, ρ_i is the density of ice, g is the acceleration due to gravity, s is the ice surface elevation, and d is the ice bed elevation.

We use surface and bed topography (also on a 5- x 5- km grid) [33] to solve for the subglacial hydrologic potential and route water down potential using the Least Cost Path (LCP) and Multiple Flow Direction algorithms [40], which allow water to be routed without requiring sink-filling. The gridded bed topography and resulting hydrologic potential have uncertainties due to survey spacing and gridding artifacts that can result in the erroneous routing of subglacial water and lead to a misinterpretation of melt quantities from echo strength anomalies. To address this uncertainty, I produce 1,000 bed topography realizations by adding white noise with a rms height of 100 m (approximate value of observed bed variations within a grid cell) to the gridded topography and produce a set of water routing models that assume uniform melt. From this collection of water routing models, I selected the models which produced a relative distribution of water

$$Z_Q = \frac{Q - \mu_Q}{\sigma_Q} \tag{5.8}$$

that most closely fits the observed relative echo strengths using the cost function Δ

$$\Delta = \sum (Z_Q - Z_\mu)^2. \tag{5.9}$$

This process selected the 50 subglacial water routing models that best explain the observed pattern of relative bed-echo strengths by routing alone (without invoking heterogenous basal melting).

5.4.4 Estimated basal melt rates and geothermal flux

Each of these pathways were used to create a least-squares fit [67] for the relative melt Z_F required to reproduce the observed mean corrected relative echo strength for each of water routing models, given by

$$Z_F = \frac{M_F - \mu_F}{\sigma_F}, \tag{5.10}$$

where M_F is the fitted melt at each cell, μ_F is the spatial average of M_F, and σ_F is the spatial standard deviation of M_F. From the relative distribution of melt, I use the mean melt-water quantities μ_J from an ice sheet model of Thwaites Glacier [46] that include frictional melting, horizontal advection, and an assumed uniform geothermal flux of 70 mW/m^2 to scale my results so that the total radar inferred quantity is equal to the total modeled melt-water quantity for the upstream region of the Thwaites Glacier. I also scale the variance of the radar inferred melt-water by the spatial variance of routed subglacial water σ_Q using the same total melt [46]. The resulting melt-water quantity estimated from the radar M is given by

$$M = Z_F \sigma_Q \left(\frac{\mu_J}{\mu_Q} \right) + \mu_J. \tag{5.11}$$

From this inferred melt, I subtracted the mean value for the net modeled frictional and advective contributions to basal melt [46] and calculate the geothermal flux G required to produce the remaining melt given by

$$G = (M - \mu_J) L_w + 70 mW/m^2, \tag{5.12}$$

where L_w is the latent heat of fusion of water and 70 mW/m^2 is the uniform geothermal heat flux used in the ice sheet model [46]. I estimate the uncertainty on the inferred geothermal flux (ΔG) to be given by

$$\Delta G = \sigma_Q \left(\frac{\mu_J}{\mu_Q} \right) L_w. \tag{5.13}$$

Chapter 6

Conclusion

Taken together, the results presented in the previous four chapters provide new insight into the past, present, and future evolution of Thwaites Glacier and its subglacial hydrology. Paleo Thwaites Glacier once shared a single grounding line with paleo Pine Island Glacier on the outer continental shelf of the ASE (Figure 1.9a) [49]. At that time, it was underlain by deformable sediments [43] that would have supported relatively shallow surface slopes and provided the sedimentary setting for a distributed canal system with low water speeds. For distributed subglacial canals, the speed of water (U_{canal}) is given by

$$U_{canal} = \sqrt{\frac{8\rho_i g}{f_R \rho_w} h_c \sin\alpha}, \tag{6.1}$$

where ρ_i is the density of ice, ρ_w is the density of water, g is the acceleration due to gravity, f_R is a dimensionless bed roughness factor, α is the ice sheet surface slope, and h_c is the canal depth [112]. With typical values for these parameters [112], including canals 10 cm deep ($h_c = 10$ cm),

$$U_{canal} \approx 26 \text{ cm/s}. \tag{6.2}$$

Although regions of exposed bedrock existed beneath paleo Thwaites Glacier, those regions were too far inland of the grounding line to create the steep

surface slopes required for concentrated subglacial channels [112]. Therefore, the entire subglacial water system was likely composed of a distributed network capable of suspending silt grains and depositing them in basins in the exposed bedrock regions (where convergence and lack of sediment supply both encouraged deposition) (Figure 6.1a to Figure 6.1b).

Once the grounding line approached the region of exposed bedrock (Figure 6.1b), the bed rheology could support the steeper surface slopes required for a subglacial water system transition in which the downstream portion was composed of concentrated channels and the upstream portion of the water system remained a distributed network of canals. This transition would reinforce steep surface slopes in the lower trunk, since high lubrication upstream (from the distributed canals) and low lubrication downstream (from the concentrated channels), would increase the basal shear stress and surface slopes above the bedrock region. The concentrated water network would be capable of eroding any silts stored in bedrock basins due to the increase in subglacial water speed, which for a concentrated channel ($U_{channel}$) is

$$U_{channel} = \sqrt{\frac{8\rho_i g}{f_R \rho_w} r_c (\pi + 2) \sin \alpha}, \tag{6.3}$$

where r_c is the radius of the channel [112]. For the same typical values used above [112] and channels with a radius (r_c) of 10 cm (a highly conservative value (Figure 1.9b)),

$$U_{canal} \approx 500 \text{ cm/s}. \tag{6.4}$$

The erosion of silt stored in bedrock basins by the transition of the downstream

water system to concentrated channels (and the resulting increase in water speed by an order of magnitude or more) would produce a meltwater plumite deposit (like the one observed in the ASE from the paleo Pine Island retreat [116] (Figure 1.9)) at a rate limited by silt storage rather than water supply (Figure 6.1b). Similar silt units (like the one observed beneath a layer of marine sediments in Marguerite Bay [47]) may also be sedimentary indicators of paleo subglacial water systems with concentrated channels (existing $\sim$ 9.3 kya in the case of Marguerite Bay [116]).

As the contemporary Thwaites Glacier grounding line moves across the bedrock region (Figure 6.1b to Figure 6.1c), it is likely to progress in a relatively rapid, back-stepping, meltwater intensive retreat (like paleo Pine Island Glacier across the inner shelf of the ASE [49]). The pacing, frequency, and extent of these back-steps will depend on its forcings, boundary conditions, and geometry. One forcing will be warm ocean water on the continental shelf melting ice near the grounding zone [86]. The impact of this melting will be amplified by the water system transition which has redistributed more basal sheer stress to the lower trunk so that melting in this region would leave larger unbalanced forces that could result in retreat events with increased frequency and extent. The presence of elevated and spatially variable geothermal flux in the upper catchment of Thwaites Glacier is an additional forcing on the evolution and retreat of the glacier (due to the potential for large and temporarily varying upstream melt water quantities to be generated by rift-associated magmatic migration and volcanism). Any change in melt water supply to the

upstream region will result in acceleration of the ice above the distributed portion of the water system. However, a sufficiently large variation in melt water supply (as could result from a subglacial volcanic eruption) may have the potential to temporarily overwhelm the concentrated downstream region of the subglacial water system and trigger or facilitate a back-stepping episode (which could also serve as the trigger for a larger ice sheet wide unstable retreat).

Once Thwaites Glacier reaches the upper portion of its catchment (Figure 6.1c), its grounding line will be underlain by a layer of deformable sediments (with the potential to stabilize or mitigate the retreat [82, 20]). It will also be underlain by a distributed water system (with potential to reduce the stabilizing basal shear stresses and facilitate the retreat). Ultimately, the pacing, extent, and character of the eventual retreat of Thwiates Glacier and the WAIS may depend more on the details of heterogeneous hydrologic, lithologic, and geothermal basal boundary conditions than the bulk shape, speed, and ocean forcing of the ice sheet.

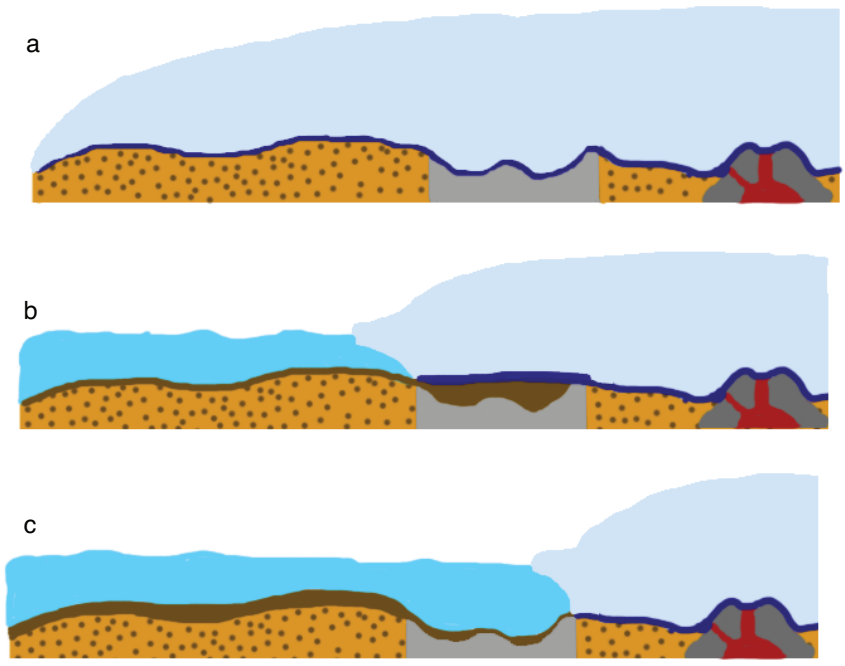

Figure 6.1: Cartoon illustrating the evolution of the hydrologic basal boundary conditions for Thwaites Glacier. (a) Paleo Thwaites Glacier, grounded on the outer continental shelf and underlain by a pervasive distributed water network, which is transporting and storing silt from the subglacial till. (b) Paleo and contemporary Thwaites Glacier grounded over a region of exposed bedrock on the inner continental shelf. The subglacial water system transitions from distributed canals upstream to concentrated channels downstream, which are eroding silt stored in bedrock basins. (c) Thwaites Glacier, once it reaches the upstream portion of the catchment and is grounded on deformable sediments with a distributed water system. In each configuration, the subglacial water system is being fed by melt from elevated and variable geothermal flux due to rift-associated magmatic migration and volcanism upstream.

List of Variables

S_c Specularity content of a bed echo

S Specular component of a bed echo

D Diffuse component of a bed echo

L Focusing aperture length

x Refraction point at the ice surface

h Aircraft survey height above the ice surface

d Ice thickness

Φ Range of scattering angles spanned at the bed

ϵ_r Relative permittivity of ice

l Englacial attenuation rate (dB/km)

RMS_w Root-mean-squared roughness of the ice/water interface

f_c Radar center frequency

c Speed of light in a vacuum

ϕ_F Range of scattering angles spanned by a Fresnel zone

D_1 Diameter of the 1st Fresnel zone

R_w Reflection coefficient for the ice/water interface

R_b Reflection coefficient for the water/bed interface

δ Skin-depth of subglacial water layer

T Thickness of subglacial water layer

σ_w Conductivity of subglacial water

μ_0 Permeability of free space

L_w Length of a subglacial water body

W_w Width of a subglacial water body

ϕ Along-track scattering angle

Θ Observation angle

k Radar wave number

S_{NS} Specularity in the North-South grid direction

S_{EW} Specularity in the East-West grid direction

A Anisotropy of specularity

S_{ave} Average specularity

Θ_{spec} Axis of symmetry for specularity

Θ_{line} Survey direction

Θ_{ice} Ice flow direction

Θ_{obs} Observation angle

H Bedform crest-to-trough height

w Bedform crest-to-crest width

$\sigma_{texture}$ Root-mean-squared roughness of the bed surface texture

σ_{bed} Root-mean-squared roughness of bedforms

σ_{total} Combined root-mean-squared roughness of bedforms and texture

γ_r Geometric spreading factor for coherent reflection

γ_s Geometric spreading factor for non-coherent scattering

P Corrected relative echo strength

Z_P Normalized relative echo strength

Φ_h Subglacial hydrologic potential

g Acceleration due to gravity

ρ_i Density of ice

ρ_w Density of water

s Ice surface elevation

Q Modeled subglacial water quantity

Z_Q Relative modeled subglacial water quantity

Δ Water routing cost function

M_F Fitted basal melt rate

Z_F Relative basal melt rate

M Melt estimated from radar

L_w Latent heat of fusion of water

μ_J Mean melt from an ice sheet model

G Geothermal flux estimated from radar

Δ_G Uncertainty in geothermal flux estimate

U_{canal} Flow speed though a distributed canal

$U_{channel}$ Flow speed though a concentrated channel

α Ice sheet surface slope

h_c Depth of a subglacial canal

f_R A dimensionless basal roughness factor

r_c Radius of a subglacial canal

Bibliography

[1] R B Alley. Water-Pressure Coupling of Sliding and Bed Deformation: I. Water System. *Journal of Glaciology*, 35(119):108–118, 1989.

[2] R B Alley, S Anandakrishnan, C R Bentley, and N Lord. A water-piracy hypothesis for the stagnation of Ice Stream C, Antarctica. *Annals of Glaciology*, 20(1):187–194, 1994.

[3] R B Alley, S Anandakrishnan, T K Dupont, B R Parizek, and D Pollard. Effect of sedimentation on ice-sheet grounding-line stability. *Science*, 315(5820):1838–41, 2007.

[4] R B Alley, T K Dupont, B R Parizek, S Anandakrishnan, D E Lawson, G J Larson, and E B Evenson. Outburst flooding and the initiation of ice-stream surges in response to climatic cooling: A hypothesis. *Geomorphology*, 75(1-2):76–89, 2006.

[5] J B Anderson and M Jakobsson. OSO0910 Scientific Party, 2010. Oden Southern Ocean 0910: Cruise Repor. In *Meddelanden från Stockholms Universitets Institution för Gelogiska Vetenskaper*, number No 341, page pp. 134. Stockholms Universitets för Gelogiska Vetenskaper, 2010.

[6] K M Assmann, A Jenkins, D R Shoosmith, D P Walker, S Jacobs, and K W Nicholls. Variability of Circumpolar Deep Water transport

onto the Amundsen Sea Continental shelf through a shelf break trough. *Journal of Geophysical Research: Oceans*, 118(12):6603–6620, 2013.

[7] J L Bamber, J L Gomez-Dans, and J A Griggs. Antarctic 1 km Digital Elevation Model (DEM) from Combined ERS-1 Radar and ICESat Laser Satellite Altimetry. *The Cryosphere*, 3(1):101–111, 2009.

[8] J L Bamber, J A Griggs, R Hurkmans, J A Dowdeswell, S P Gogineni, I M Howat, J Mouginot, J Paden, S Palmer, E Rignot, and D. Steinhage. A new bed elevation dataset for Greenland. *The Cryosphere*, 7(2):499–510, 2013.

[9] J L Bamber, R E M Riva, B Vermeersen, and A M Le Brocq. Reassessment of the Potential Sea-Level Rise from a Collapse of the West Antarctic Ice Sheet. *Science*, 324(5929):901–903, 2009.

[10] J C Behrendt. The aeromagnetic method as a tool to identify Cenozoic magmatism in the West Antarctic Rift System beneath the West Antarctic Ice Sheet—A review; Thiel subglacial volcano as possible source of the ash layer in the WAISCORE. *Tectonophysics*, 585:124–136, 2013.

[11] J C Behrendt, D D Blankenship, C A Finn, R E Bell, R E Sweeney, S M Hodge, and J M Brozena. CASERTZ aeromagnetic data reveal late Cenozoic flood basalts (?) in the West Antarctic rift system. *Geology*, 22(6):527–530, 1994.

[12] J C Behrendt, C A Finn, D D Blankenship, and R E Bell. Aeromagnetic evidence for a volcanic caldera (?) complex beneath the divide of the West Antarctic Ice Sheet. *Geophysical Research Letters*, 25(23):4385–4388, 1998.

[13] C R Bentley, D D Blankenship, D G Schultz, S T Rooney, and S Anandakrishnan. Geophysical program at Upstream B camp, Siple Coast. *Antarctic Journal of the United States*, 21(5):109, 1986.

[14] D D Blankenship, R E Bell, S M Hodge, J M Brozena, J C Behrendt, and C A Finn. Active volcanism beneath the West Antarctic ice sheet and implications for ice-sheet stability. *Nature*, pages 526–529, 1993.

[15] D D Blankenship, D L Morse, C A Finn, R E Bell, M E Peters, S D Kempf, S M Hodge, M Studinger, J C Behrendt, and J M Brozena. Geologic controls on the initiation of rapid basal motion for West Antarctic ice streams: A geophysical perspective including new airborne radar sounding and laser altimetry results. *The West Antarctic Ice Sheet: Behavior and Environment*, pages 105–121, 2001.

[16] S P Carter, D D Blankenship, D A Young, and J W Holt. Using radar-sounding data to identify the distribution and sources of subglacial water: application to Dome C, East Antarctica. *Journal of Glaciology*, 55(194):1025–1040, 2009.

[17] S P Carter, D D Blankenship, D A Young, M E Peters, J W Holt, and M J Siegert. Dynamic distributed drainage implied by the flow evolution

of the 1996–1998 Adventure Trench subglacial lake discharge. *Earth and Planetary Science Letters*, 283(1-4):24–37, 2009.

[18] G A Catania and C Paola. Braiding under glass. *Geology*, 29(3):259–262, 2001.

[19] J L Chen, C R Wilson, D D Blankenship, and B D Tapley. Accelerated Antarctic ice loss from satellite gravity measurements. *Nature Geoscience*, 2(12):859–862, 2009.

[20] K Christianson, B R Parizek, R B Alley, H J Horgan, R W Jacobel, S Anandakrishnan, B A Keisling, B D Craig, and A Muto. Ice sheet grounding zone stabilization due to till compaction. *Geophysical Research Letters*, 40(20):5406–5411, 2013.

[21] J A Church, J M Gregory, N J White, S M Platten, and J X Mitrovica. Understanding and projecting sea level change. *Oceanography*, 24(2):130, 2011.

[22] G D Clow, K Cuffey, and E Waddington. High heat-flow beneath the central portion of the West Antarctic Ice Sheet. *Eos Transactions, AGU Fall Meeting Supplement*, 2012.

[23] H F Corr and D G Vaughan. A recent volcanic eruption beneath the West Antarctic Ice Sheet. *Nature Geoscience*, 1(2):122–125, 2008.

[24] T T Creyts and C G Schoof. Drainage through subglacial water sheets. *Journal of Geophysical Research*, 114(F4), 2009.

[25] J A Dowdeswell and S Evans. Investigations of the form and flow of ice sheets and glaciers using radio-echo sounding. *Reports on Progress in Physics*, 67(10):1821–1861, 2004.

[26] J A Dowdeswell, D Ottesen, J Evans, C O'Cofaigh, and J B Anderson. Submarine glacial landforms and rates of ice-stream collapse. *Geology*, 36(10):819, 2008.

[27] D J Drewry. Comparison of electromagnetic and seismic-gravity ice thickness measurements in East Antarctica. *Journal of Glaciology*, 15:137–150, 1975.

[28] S Evans and G Robin. Glacier depth-sounding from the air. *Nature*, 210, 1966.

[29] S Evans and B Smith. A radio echo equipment for depth sounding in polar ice sheets. *Journal of Physics E: Scientific Instruments*, 2(2):131, 1969.

[30] M Fahnestock, W Abdalati, I Joughin, J M Brozena, and S P Gogineni. High geothermal heat flow, basal melt, and the origin of rapid ice flow in central Greenland. *Science*, 294(5550):2338–2342, 2001.

[31] L Favier, G Durand, S L Cornford, G H Gudmundsson, O Gagliardini, F Gillet-Chaulet, T Zwinger, A J Payne, and A M Le Brocq. Retreat of Pine Island Glacier controlled by marine ice-sheet instability. *Nature Climate Change*, 4:117–121, 2014.

[32] A G Fountain and J S Walder. Water flow through temperate glaciers. *Reviews of Geophysics*, 36(3):299–328, 1998.

[33] P Fretwell, H D Pritchard, D G Vaughan, L Bamber, N E Barrand, R E Bell, C Bianchi, R G Bingham, D D Blankenship, G Casassa, et al. Bedmap2: improved ice bed, surface and thickness datasets for Antarctica. *The Cryosphere*, 7(1):375–393, 2013.

[34] A M Gades, C F Raymond, H Conway, and R W Jacobel. Bed properties of Siple Dome and adjacent ice streams, West Antarctica, inferred from radio-echo sounding measurements. *Journal of Glaciology*, 46(152), 2000.

[35] S P Gogineni, T Chuah, C Allen, K C Jezek, and R K Moore. An improved coherent radar depth sounder. *Journal of Glaciology*, 44(148):659–669, 1998.

[36] J A Griggs and J L Bamber. A new 1 km digital elevation model of Antarctica derived from combined radar and laser data – Part 2: Validation and error estimates. *The Cryosphere*, 3(1):113–123, 2009.

[37] P Gudmandsen. *Electromagnetic probing of ice*, page 321. Golem Press, 1971.

[38] F Heliere, C C Lin, F Heliere, H Corr, and D G Vaughan. Radio Echo Sounding of Pine Island Glacier, West Antarctica: Aperture Synthesis

Processing and Analysis of Feasibility From Space. *IEEE Transactions on Geoscience and Remote Sensing*, 45(8):2573–2582, 2007.

[39] C D Hillenbrand, M Melles, G Kuhn, and R D Larter. Marine geological constraints for the grounding-line position of the Antarctic Ice Sheet on the southern Weddell Sea shelf at the Last Glacial Maximum. *Quaternary Science Reviews*, 32:25–47, 2012.

[40] P Holmgren. Multiple flow direction algorithms for runoff modelling in grid based elevation models: An empirical evaluation. *Hydrological Processes*, 8(4):327–334, 1994.

[41] J W Holt, D D Blankenship, D L Morse, D A Young, M E Peters, S D Kempf, T G Richter, D G Vaughan, and H F Corr. New boundary conditions for the West Antarctic Ice Sheet: Subglacial topography of the Thwaites and Smith glacier catchments. *Geophysical Research Letters*, 33(9):L09502, 2006.

[42] M Jakobsson, J B Anderson, F O Nitsche, J A Dowdeswell, R Gyllencreutz, N Kirchner, R Mohammad, M O Regan, R B Alley, S Anandakrishnan, B Eriksson, R Fernandez, T Stolldorf, R Minzoni, W Majewski, and M O'Regan. Geological record of ice shelf break-up and grounding line retreat, Pine Island Bay, West Antarctica. *Geology*, 39(7):691–694, 2011.

[43] M Jakobsson, J B Anderson, F O Nitsche, R Gyllencreutz, A E Kirshner, N Kirchner, M O'Regan, R Mohammad, and B Eriksson. Ice

sheet retreat dynamics inferred from glacial morphology of the central Pine Island Bay Trough, West Antarctica. *Quaternary Science Reviews*, 38:1–10, 2012.

[44] A Jenkins, P Dutrieux, S S Jacobs, S D McPhail, J R Perrett, A T Webb, and D White. Observations beneath Pine Island Glacier in West Antarctica and implications for its retreat. *Nature*, 3(7):468–472, 2010.

[45] J S Johnson, M J Bentley, J A Smith, R C Finkel, D H Rood, K Gohl, G Balco, R D Larter, and J M Schaefer. Rapid Thinning of Pine Island Glacier in the Early Holocene. *Science*, 343(6174):999 – 1001, 2014.

[46] I R Joughin, S Tulaczyk, J L Bamber, D D Blankenship, J W Holt, T Scambos, and D G Vaughan. Basal conditions for Pine Island and Thwaites Glaciers, West Antarctica, determined using satellite and airborne data. *Journal of Glaciology*, 55(190):245–257, 2009.

[47] D S Kennedy and J B Anderson. Glacial-marine sedimentation and Quaternary glacial history of Marguerite Bay, Antarctic Peninsula. *Quaternary Science Reviews*, 31:255–276, 1989.

[48] E C King, R C Hindmarsh, and C R Stokes. Formation of mega-scale glacial lineations observed beneath a West Antarctic ice stream. *Nature Geoscience*, 2(8):585–588, 2009.

[49] A E Kirshner, J B Anderson, M Jakobsson, M O'Regan, W Majewski, and F O Nitsche. Post-LGM deglaciation in Pine Island Bay, West

Antarctica. *Quaternary Science Reviews*, 38:11–26, 2012.

[50] Eugene F Knott, John F Shaeffer, and Michael T Tuley. *Radar Cross Section*. SciTech Publishing, Raleigh, 2004.

[51] E Larour, M Morlighem, H Seroussi, J Schiermeier, and E Rignot. Ice flow sensitivity to geothermal heat flux of Pine Island Glacier, Antarctica. *Journal of Geophysical Research: Earth Surface*, 117(F4), 2012.

[52] R D Larter, A G Graham, and K Gohl. Subglacial bedforms reveal complex basal regime in a zone of paleo–ice stream convergence, Amundsen Sea embayment, West Antarctica. *Geology*, 37(5):411–414, 2009.

[53] A M Le Brocq, A J Payne, M J Siegert, and R B Alley. A subglacial water-flow model for West Antarctica. *Journal of Glaciology*, 55(193):879–888, 2009.

[54] H Lee, C Shum, I M Howat, A Monaghan, Y Ahn, J Duan, J-Y Guo, C-Y Kuo, and L Wang. Continuously accelerating ice loss over Amundsen Sea catchment, West Antarctica, revealed by integrating altimetry and GRACE data. *Earth and Planetary Science Letters*, 321-322:74–80, 2012.

[55] J J Legarsky, S P Gogineni, and T L Akins. Focused synthetic aperture radar processing of ice-sounder data collected over the Greenland Ice Sheet. *IEEE Transactions on Geoscience and Remote Sensing*, 39(10):2109–2117, 2001.

[56] W E LeMasurier and F A Wade. Fumarolic activity in Marie Byrd Land, Antarctica. *Science*, 162(3851):352–352, 1968.

[57] C Leuschen and R Plumb. A matched-filter approach to wave migration. *Journal of Applied Geophysics*, 43(2):271–280, 2000.

[58] S J Livingstone, C O'Cofaigh, C R Stokes, C-D Hillenbrand, A Vieli, and S Jamieson. Antarctic palaeo-ice streams. *Earth Science Reviews*, 111:90–128, 2012.

[59] A C Lough, D A Wiens, C G Barcheck, S Anandakrishnan, R C Aster, D D Blankenship, A D Huerta, A Nyblade, D A Young, and Terry J Wilson. Seismic detection of an active subglacial magmatic complex in Marie Byrd Land, Antarctica. *Nature Geoscience*, 6:1031 – 1035, 2013.

[60] A L Lowe and J B Anderson. Evidence for abundant subglacial meltwater beneath the paleo-ice sheet in Pine Island Bay, Antarctica. *Journal of Glaciology*, 49(164):125–138, 2003.

[61] Ashley L Lowe and John B Anderson. Reconstruction of the West Antarctic Ice Sheet in Pine Island Bay during the Last Glacial Maximum and its subsequent retreat history. *Journal of Glaciology*, 49(164):1879–1897, 2002.

[62] J A MacGregor, G A Catania, H Conway, D M Schroeder, I J, D A Young, S D Kempf, and D D Blankenship. Weak bed control of the

eastern shear margin of Thwaites Glacier, West Antarctica. *Journal of Glaciology*, 59(217):900–912, 2013.

[63] J A MacGregor, D P Winebrenner, H Conway, K Matsuoka, P A Mayewski, and G D Clow. Modeling englacial radar attenuation at Siple Dome, West Antarctica, using ice chemistry and temperature data. *Journal of Geophysical Research*, 112(F3):F03008, 2007.

[64] K Matsuoka. Pitfalls in radar diagnosis of ice-sheet bed conditions: Lessons from englacial attenuation models. *Geophysical Research Letters*, 38(5):L05505, 2011.

[65] K Matsuoka, J A MacGregor, and F Pattyn. Predicting radar attenuation within the Antarctic ice sheet. *Earth and Planetary Science Letters*, 359-360:173–183, 2012.

[66] C F Maule, M E Purucker, N Olsen, and K Mosegaard. Heat flux anomalies in Antarctica revealed by satellite magnetic data. *Science*, 309(5733):464–467, 2005.

[67] W Menke. *Geophysical data analysis: Discrete inverse theory*. Academic Press, 2012.

[68] R K Moore. Modern coherent radar for ice-sheet sounding. *Antarctic Journal of the United States*, 22(5):83, 1987.

[69] A Moussessian, R L Jordan, E Rodriguez, A Safaeinili, T L Akins, W N Edelstein, Y Kim, and S P Gogineni. A new coherent radar for ice

sounding in Greenland. In *Geoscience and Remote Sensing Symposium, 2000*, volume 2, pages 484–486. IEEE, 2000.

[70] A Muto, S Anandakrishnan, and R B Alley. Subglacial bathymetry and sediment layer distribution beneath the Pine Island Glacier ice shelf, West Antarctica, modeled using aerogravity and autonomous underwater vehicle data. *Annals of Glaciology*, 54(64):27–32, 2013.

[71] S K Nayar, K Ikeuchi, and T Kanade. Surface reflection: physical and geometrical perspectives. *IEEE Transactions on Pattern Analysis*, 13(7):611–634, 1991.

[72] G Ng, 2011.

[73] F O Nitsche, K Gohl, R D Larter, C-D Hillenbrand, G Kuhn, J A Smith, S Jacobs, J B Anderson, and M Jakobsson. Paleo ice flow and subglacial meltwater dynamics in Pine Island Bay, West Antarctica. *The Cryosphere*, 7(1):249–262, 2013.

[74] Z Deretsky NSF, 2012.

[75] C O'Cofaigh and C J Pudsey. Evolution of subglacial bedforms along a paleo-ice stream, Antarctic Peninsula continental shelf. *Geophysical Research Letters*, 29(8):1–4, 2002.

[76] J A Ogilvy. *Theory of wave scattering from random rough surfaces*. A. Hilger, Bristol, 1991.

[77] G K Oswald. Investigation of sub-ice bedrock characteristics by radio-echo sounding. *Journal of Glaciology*, 5(73):975, 1975.

[78] G K Oswald and S P Gogineni. Recovery of subglacial water extent from Greenland radar survey data. *Journal of Glaciology*, 54(184):94–106, 2008.

[79] G K Oswald and G D Robin. Lakes Beneath the Antarctic Ice Sheet. *Nature*, 245(5423):251–254, 1973.

[80] J Paden, T Akins, D Dunson, C Allen, and S P Gogineni. Ice-sheet bed 3-D tomography. *Journal of Glaciology*, 56(195):3–11, 2010.

[81] J M Palais, P R Kyle, W C McIntosh, and D Seward. Magmatic and phreatomagmatic volcanic activity at Mt. Takahe, West Antarctica, based on tephra layers in the Byrd ice core and field observations at Mt. Takahe. *Journal of Volcanology and Geothermal Research*, 35(4):295–317, 1988.

[82] B R Parizek, K Christianson, S Anandakrishnan, R B Alley, R T Walker, R A Edwards, D S Wolfe, G T Bertini, S K Rinehart, R A Bindschadler, and S Nowicki. Dynamic (In)stability of Thwaites Glacier, West Antarctica. *Journal of Geophysical Research: Earth Surface*, 118:638–655, 2013.

[83] M E Peters, D D Blankenship, S P Carter, S D Kempf, D A Young, and J W Holt. Along-Track Focusing of Airborne Radar Sounding

Data From West Antarctica for Improving Basal Reflection Analysis and Layer Detection. *IEEE Transactions on Geoscience and Remote Sensing*, 45(9):2725–2736, 2007.

[84] M E Peters, D D Blankenship, and D L Morse. Analysis techniques for coherent airborne radar sounding: Application to West Antarctic ice streams. *Journal of Geophysical Research*, 110(B6):B06303, 2005.

[85] H D Pritchard, R J Arthern, D G Vaughan, and L A Edwards. Extensive dynamic thinning on the margins of the Greenland and Antarctic ice sheets. *Nature*, 461(7266):971–975, 2009.

[86] H D Pritchard, S R Ligtenberg, H A Fricker, D G Vaughan, M R van den Broeke, and L Padman. Antarctic ice-sheet loss driven by basal melting of ice shelves. *Nature*, 484(7395):502–5, 2012.

[87] G Raju and R K Moore. A matched-filter technique for removing hyperbolic effects due to point scatterers: Simulation and application on Antarctic radar data. *IEEE Transactions on Geoscience and Remote Sensing*, 28(4):726–729, 1990.

[88] R K Raney. The delay/Doppler radar altimeter. *IEEE Transactions on Geoscience and Remote Sensing*, 36(5):1578–1588, 1998.

[89] R K Raney. Radar ice sounder with parallel Doppler processing, February 13 2001. US Patent 6,188,348.

[90] R K Raney, B L Gotwels, and J R Jensen. Optimal processing of radar ice sounding data. In *Geoscience and Remote Sensing Symposium, 1999*, volume 1, pages 92–94. IEEE, 1999.

[91] E Rignot, J L Bamber, M R van den Broeke, C Davis, Y Li, W J van de Berg, and E van Meijgaard. Recent Antarctic ice mass loss from radar interferometry and regional climate modeling. *Nature Geoscience*, 1(2):106–110, 2008.

[92] E Rignot, S Jacobs, J Mouginot, and B Scheuchl. Ice-shelf melting around Antarctica. *Science*, 341(6143):266–70, 2013.

[93] E Rignot, J Mouginot, and B Scheuchl. Ice flow of the Antarctic ice sheet. *Science*, 333(6048):1427–1430, 2011.

[94] V Sarma, N Prasad, and P Rajendra Prasad. The effect of hydrogeology on variations in the electrical conductivity of groundwater fluctuations. *Journal of Hydrology*, 44(1):81–87, 1979.

[95] C G Schoof. Ice sheet grounding line dynamics: Steady states, stability, and hysteresis. *Journal of Geophysical Research*, 112(F3):1–19, 2007.

[96] C G Schoof. Ice-sheet acceleration driven by melt supply variability. *Nature*, 468(7325):803–806, 2010.

[97] D M Schroeder, D D Blankenship, and D A Young. Evidence for a water system transition beneath Thwaites Glacier, West Antarctica. *Pro-*

ceedings of the National Academy of Sciences of the United States of America, 110(30):12225–8, 2013.

[98] D G Schultz, L A Powell, and C R Bentley. A digital radar system for echo studies on ice sheets. *Annals of Glaciology*, 9:206–210, 1987.

[99] N M Shapiro and M H Ritzwoller. Inferring surface heat flux distributions guided by a global seismic model: particular application to Antarctica. *Earth and Planetary Science Letters*, 223(1):213–224, 2004.

[100] M K Shepard, B A Campbell, M H Bulmer, T G Farr, L R Gaddis, and J J Plaut. The roughness of natural terrain: a planetary and remote sensing perspective. *Journal of Geophysical Research*, 106:777–795, 2001.

[101] M J Siegert, S Carter, I Tabacco, S Popov, and D D Blankenship. A revised inventory of Antarctic subglacial lakes. *Antarctic Science*, 17(3):453–460, 2005.

[102] M J Siegert and J K Ridley. Determining basal ice-sheet conditions in the Dome C region of East Antarctica using satellite radar altimetry and airborne radio-echo sounding. *Journal of Glaciology*, 44(146):1–8, 1998.

[103] A M Smith, T A Jordan, F Ferraccioli, and R G Bingham. Influence of subglacial conditions on ice stream dynamics: Seismic and potential field data from Pine Island Glacier, West Antarctica. *Journal of Geophysical Research: Solid Earth*, 118(4):1471–1482, 2013.

[104] S Solomon, D Qin, M Manning, Z Chen, M Marquis, K B Averyt, M Tignor, and H L Miller. The physical science basis. *Contribution of Working Group I to the Fourth Assessment Report of the Intergovernmental Panel on Climate Change*, pages 235–337, 2007.

[105] J D Stanford, R Hemingway, E J Rohling, P G Challenor, M Medina-Elizalde, and A J Lester. Sea-level probability for the last deglaciation: A statistical analysis of far-field records. *Global and Planetary Change*, 79(3):193–203, 2011.

[106] L A Stearns, B E Smith, and G S Hamilton. Increased flow speed on a large East Antarctic outlet glacier caused by subglacial floods. *Nature Geoscience*, 1(12):827–831, 2008.

[107] B O Steenson. *Radar Methods for the Exploration of Glaciers*. CIT theses. California Institute of Technology, 1951.

[108] K J Tinto and R E Bell. Progressive unpinning of Thwaites Glacier from newly identified offshore ridge: Constraints from aerogravity. *Geophysical Research Letters*, 38(20), 2011.

[109] D G Vaughan, H F Corr, F Ferraccioli, N Frearson, A O'Hare, D Mach, J W Holt, D D Blankenship, D L Morse, and D A Young. New boundary conditions for the West Antarctic ice sheet: Subglacial topography beneath Pine Island Glacier. *Geophysical Research Letters*, 33(9):L09501, 2006.

[110] S W Vogel and S Tulaczyk. Ice-dynamical constraints on the existence and impact of subglacial volcanism on West Antarctic ice sheet stability. *Geophysical Research Letters*, 33(23), 2006.

[111] H Von Storch and F W Zwiers. *Statistical analysis in climate research*. Cambridge University Press, 2001.

[112] J S Walder and A Fowler. Channelized subglacial drainage over a deformable bed. *Journal of Glaciology*, 40(134):3–15, 1994.

[113] R T Walker, B R Parizek, R B Alley, S Anandakrishnan, K L Riverman, and K Christianson. Ice-shelf tidal flexure and subglacial pressure variations. *Earth and Planetary Science Letters*, 361(0):422 – 428, 2013.

[114] J Weertman. Stability of Ice-Age Ice Sheets. *Journal of Geophysical Research*, 66(11):3783–3792, 1961.

[115] J S Wellner, D C Heroy, and J B Anderson. The death mask of the Antarctic ice sheet: Comparison of glacial geomorphic features across the continental shelf. *Geomorphology*, 75(1-2):157–171, 2006.

[116] A E Witus, C M Branecky, J B Anderson, W Szczuciniski, D M Schroeder, D D Blankenship, and M Jakobsson. Meltwater Intensive Glacial Retreat in Polar Environments and Investigation of Associated Sediments: Example from Pine Island Bay West Antarctica. *Quaternary Science Reviews*, 85:99 – 118, 2014.

[117] A P Wright and M J Siegert. The identification and physiographical setting of Antarctic subglacial lakes: An update based on recent discoveries. In *Antarctic Subglacial Aquatic Environments*, volume 192 of *Geophysical Monograph Series*, pages 9–26. AGU, 2011.

[118] X Wu, K C Jezek, E Rodriguez, S P Gogineni, F Rodriguez-Morales, and A Freeman. Ice sheet bed mapping with airborne SAR tomography. *IEEE Transactions on Geoscience and Remote Sensing*, 49(10):3791–3802, 2011.

Vita

Dustin Matthew Schroeder attended Solon High School in Solon, OH. Summer 2002, he was a research assistant in particle astrophysics at Case Western Reserve University in Cleveland, OH. Fall 2002, he entered Bucknell University in Lewisburg, PA. Summer 2004, he was a research assistant in astrophysical instrumentation at the Harvard-Smithsonian Center for Astrophysics in Cambridge, MA. Summer 2005, he was a research assistant in BioMEMs at the Cleveland Clinic in Cleveland, OH. Summer 2006 through spring 2007, he was a research assistant in antenna design at Bucknell University. He received a Bachelor of Science in electrical engineering and Bachelor of Arts in physics from Bucknell University in May 2007. 2007-2008, he was an engineer at Freescale Semiconductor in Austin, TX. Fall 2008, he entered graduate school at the University of Texas at Austin. 2009 - 2014, he was an NSF GRFP Fellow. Winters 2008-2011, he participated in three Antarctic field seasons as lead RF field engineer with the ICECAP project. Spring 2011, he was a research assistant in radar sounding theory at the Johns Hopkins University Applied Physics Lab.

Permanent address: 3406 B Duval Street
Austin, Texas 78705

This dissertation was typeset with LaTeXby the author.